Bioactive Materials 41 (2024) 293–311

Contents lists available at ScienceDirect

Bioactive Materials

journal homepage: www.keaipublishing.com/en/journals/bioactive-materials

Insight the long-term biodegradable Mg-RE-Sr alloy for orthopaedics implant via friction stir processing

Yixing Zhu [a,b], Mengran Zhou [a,b,*], Weikang Zhao [c,**], Yingxin Geng [a,b], Yujie Chen [d], Han Tian [a,b], Yifan Zhou [a,b], Gaoqiang Chen [a,b], Ruizhi Wu [d], Yufeng Zheng [e], Qingyu Shi [a,b]

[a] State Key Laboratory of Clean and Efficient Turbomachinery Power Equipment, Department of Mechanical Engineering, Tsinghua University, Beijing, 100084, PR China
[b] Key Laboratory for Advanced Materials Processing Technology, Ministry of Education, Beijing, 100084, PR China
[c] Department of Orthopedics, The First Affiliated Hospital of Chongqing Medical University, Chongqing, 400016, PR China
[d] Key Laboratory of Superlight Materials & Surface Technology (Ministry of Education), Harbin Engineering University, Harbin, 150001, PR China
[e] School of Materials Science and Engineering, Peking University, Beijing, 100871, PR China

ARTICLE INFO

Keywords:
Magnesium alloy
Friction stir processing
Microstructural evolution
Biodegradable
Biocompatibility

ABSTRACT

Magnesium alloys, noted for their substantial mechanical strength and exceptional biocompatibility, are increasingly being considered for use in biodegradable implants. However, their rapid degradation and significant hydrogen release have limited their applications in orthopaedics. In this study, a novel Mg-RE-Sr alloy was created by friction stir processing to modify its microstructure and enhance its degradation performance. Through microstructural characterization, the friction stir processing effectively refined the grains, accelerated the re-dissolution of precipitates, and ensured a uniform distribution of these phases. The processed alloy demonstrated improved comprehensive properties, with an *in vitro* corrosion rate of approximately 0.4 mm/y and increases in ultimate tensile strength and elongation by 37 % and 166 %, respectively. Notably, *in vivo* experiments involving a rat subcutaneous implantation model revealed a slower degradation rate of 0.09 mm/y and a uniform degradation process, basically achieving the requirements for ideal performance in orthopaedic applications. The superior degradation characteristics were attributed to the synergistic effect of attenuated galvanic corrosion and the formation of a dense $Y(OH)_3/Y_2O_3$ film induced by an exceptional microstructure with a highly solid-soluted matrix and uniformly refined precipitates. Meanwhile, the alloys exhibited excellent biocompatibility and did not cause undesirable inflammation or produce toxic degradation products. These improvements in biocompatibility and degradation characteristics indicate great promise for the use of this friction stir processed alloy in osteosynthesis systems in the clinical setting.

1. Introduction

Magnesium (Mg) and its alloys are increasingly recognized as promising materials in the field of biodegradable materials, due to their sufficient mechanical strength and biocompatibility [1,2]. Crucially, Mg is not only essential for human health, playing several vital physiological roles [3,4], but Mg alloys also demonstrate mechanical characteristics similar to those of human bone, with Young's modulus around 45 GPa [5,6], which closely matches that of human bone (20–27 GPa) [7]. This similarity provides a superior load-bearing capacity, which can effectively prevent stress shielding of the bone caused by the mismatch of Young's modulus [8,9]. Furthermore, various *in vivo* studies have shown that Mg^{2+} ions, released during the degradation of these alloys, can enhance osteogenesis [10,11]. Therefore, the amalgamation of these distinctive benefits makes Mg alloys a highly preferable option for orthopedic implant applications.

Over the last two decades, significant progress has been made in the development of Mg-based alloys for biodegradable implants. Initially, researchers employed pure Mg in cardiovascular and orthopedic implants to repair damaged tissues and organs [12]. However, the primary

Peer review under responsibility of KeAi Communications Co., Ltd.
* Corresponding author. State Key Laboratory of Clean and Efficient Turbomachinery Power Equipment, Department of Mechanical Engineering, Tsinghua University, Beijing, 100084, PR China.
** Corresponding author.
E-mail addresses: zhoumr888@mail.tsinghua.edu.cn (M. Zhou), weikangzhao90@hospital.cqmu.edu.cn (W. Zhao).

https://doi.org/10.1016/j.bioactmat.2024.07.021
Received 6 January 2024; Received in revised form 6 June 2024; Accepted 15 July 2024

limitation of pure Mg in these applications is its low mechanical strength, which is insufficient to withstand physiological loads on the human body [13]. To address this, various alloying elements, such as zinc (Zn) [2], calcium (Ca) [14,15], strontium (Sr) [16], silicon (Si) [17], zirconium (Zr) [18], and rare earth (RE) [19], have been integrated into the Mg matrix to enhance its mechanical properties. Among these, Mg-RE alloys have garnered substantial interest owing to their superior mechanical strength, castability, and other comprehensive properties [20]. A notable milestone was achieved in 2013 when the MAGNEZIX® (WE43) screw, an Mg alloy device, received the Conformity with European (CE) mark, achieving the first clinical approval of a Mg alloy medical device, thereby broadening the scope of Mg-RE alloys in biomedical engineering [21]. However, these biomedical Mg-RE alloys, containing elements such as Nd, Y, and Ce, introduce intermetallic phases by these RE elements, which in turn accelerate degradation rates through micro-galvanic corrosion [22,23]. Feng et al. [24] investigated the impact of the secondary phase on the micro-galvanic corrosion of the as-cast WE43 alloy. Their findings confirmed that the secondary phases, acting as micro-anodes, significantly accelerated the galvanic corrosion process, resulting in a severe non-uniform corrosion process. Sudholz et al. [22] presented a report on the anti-corrosion properties of a series of Mg–Y alloys with varying concentrations of Y. Their results indicated a substantial increase in the corrosion rate corresponding to an increase in Y content. In general, Mg-RE alloys exhibit rapid degradation rates (approximately 1–15 mm/y), which fall short of the requirements for implant applications in biological systems. Such rapid corrosion can compromise the mechanical integrity of implants before bone or organ healing, and excessive hydrogen production can lead to tissue inflammation and subcutaneous swelling [1,12]. For orthopedic biodegradable implants, an ideal degradation period of 12–24 months is anticipated [25,26].

Uniform degradation and superior corrosion resistance are essential qualities of Mg matrices and are considered fundamental to the advancement and popularization of biological Mg alloys. Achieving these characteristics requires precise control of the microstructure of the Mg alloy matrix. Severe plastic deformation (SPD) is well known for its ability to produce Mg alloys with evenly distributed precipitates and refined grains, which is advantageous for achieving more uniform corrosion in bio-Mg alloys. This uniformity is attributed to the reduced galvanic corrosion and formation of dense surface films [27,28]. Prior studies have explored the application of SPD methods to modify the microstructure and improve the overall properties of biomedical Mg alloys [29,30]. Among SPD techniques, friction stir processing (FSP) exhibits advantages in generating fine-grained structures and uniform precipitates [31–33]. Mansoor et al. [34] reported a ZK60 alloy with an ultrafine grain microstructure, finer precipitates, and strong basal texture by multi-pass FSP. The processed Mg alloy exhibited high yield strength (>300 MPa) and adequate ductility (>10 %). Similarly, Zhu et al. [35] achieved synergistic optimization of the strength (increased by 41.3 %), ductility (increased by 21.8 %), and corrosion (decreased by 64.5 %) in a Mg–Li–Al–Zn alloy through cross-pass FSP. Liu et al. [36] examined the effects of microstructure on the corrosion resistance of AZ91 Mg alloys post-FSP treatment, including galvanic corrosion and surface passivity. Similarly, Shunmugasamy et al. [37] successfully engineered a microstructure with uniformly distributed precipitates and refined grains of a biodegradable Mg–Zn-RE-Zr alloy after FSP, which simultaneously enhanced both the corrosion resistance and mechanical properties of the alloy. The *in vivo* corrosion rate of the alloy after FSP was measured at 0.7 mm/y, which was lower than that of numerous conventional Mg alloys. In fact, the FSP technique holds considerable promise for creating the desired microstructural and property gradients in Mg alloys, potentially enabling the processing of large-scale materials in the biomedical field using a horizontal multi-pass approach [38–40].

Recently, strontium (Sr), recognized as an osteopromotive element, has been the subject of extensive research, owing to its biological and mechanical benefits. The addition of minor Sr can refine the grains of Mg alloys, which effectively enhances both the mechanical and anti-corrosion properties owing to grain refinement [41,42]. Moreover, it has been validated that Sr can enhance cell replication and inhibit bone resorption [16,43]. In this study, we innovatively incorporated additional Sr into an Mg-RE alloy to augment its biocompatibility. Specifically, an alloy with 1 wt% Sr was integrated into the established biomedically safe WE43 Mg alloy, serving as the foundational material. Subsequently, this alloy underwent FSP, leading to a novel microstructure containing refined grains, a highly solid-soluted matrix, and a homogenous distribution of the precipitated phases. This processing resulted in the alloy exhibiting remarkable improvements in strength, both *in vitro* and *in vivo* degradation rates, and in biological compatibility.

2. Experimental

2.1. Preparation of materials

In this study, pure Mg, Mg-30 wt% RE (Y, Nd, and Gd), Mg-20 wt% Zr, and Mg-20 wt% Sr master alloys were utilized to prepare the implant base material, denoted as the WE43-1 wt%Sr alloy (designated as WEJ431). The material synthesis involved smelting these alloys using an electrical resistance furnace, conducted under a protective atmosphere of CO_2 and 0.5 % SF_6 mixed gas within a graphite crucible to obtain ingot casting. The specific chemical composition of the WEJ431 alloy was meticulously analyzed using inductively coupled plasma optical emission spectroscopy (ICP-OES), and the results are presented in Table 1. Subsequently, the cast ingot underwent precision machining via wire electrical discharge machining (EDM) to produce flat plates measuring 200 mm × 65 mm × 4 mm, which served as the starting material for further processing. Before the FSP, a thorough preparation step was performed. This involved meticulous polishing of all plate surfaces using abrasive paper up to a fineness of #4000 to eliminate any oxidation layers generated during the EDM process. The FSP procedure was executed using a specialized tool with a shoulder diameter of 15 mm and a probe length and diameter of 2.8 mm and 6 mm, respectively. To investigate the impact of the heat input, FSP was conducted at tool rotation speeds of 300, 500, 800, and 1200 rpm. The FSP operations were consistently performed at a constant processing speed of 50 mm/min. For ease of reference, the samples derived from the base metal, with tool rotation speeds of 300, 500, 800, and 1200 rpm, were denoted as "BM", "FSP-300", "FSP-500", "FSP-800", and "FSP-1200", respectively. To facilitate subsequent microstructural, mechanical, *in vitro*, and *in vivo* degradation assessments, the test specimens were extracted along the processing direction from the center in the stir zone of the processed samples. A schematic illustration of the FSP procedure and corresponding configurations of the test specimens is presented in Supplementary Fig. S1. All the samples were polished to approximately 1 mm from the top surface to ensure a uniform structure of the FSP-processed surface.

2.2. Microstructural and mechanical characterization

The microstructure characterization of the alloys before and after FSP was conducted using scanning electron microscopy (SEM, Zeiss, Gimini-300) with a back-scattered electron microscope. Chemical compositions were tested by energy-dispersive X-ray spectroscopy (EDS, Oxford). Before examination, the samples underwent a meticulous metallographic preparation process. This involved mechanical grinding with SiC paper up to 4000 grit, followed by polishing with a colloidal silica suspension (Struers OPS, 0.25 μm). Chemical etching was performed using a solution composed of 10 g picric acid, 25 mL acetic acid, 175 mL ethanol, and 25 mL distilled water prior to SEM observation and EDS analysis. The size statistics were measured by the intercept procedure using Image-Pro Plus 6.0 to estimate the distribution of the precipitated particles. The crystal orientation and grain size of the

Table 1
Chemical composition of as-prepared WEJ431 alloy.

Alloy	Chemical composition (in wt.%)							
	Y	Nd	Gd	Sr	Zr	Zn	Ca	Mg
WEJ431	3.702	2.028	1.124	0.707	0.355	0.244	0.0718	Bal.

samples were statistically analyzed using electron back-scattered diffraction (EBSD). For EBSD, an electrolytic polishing step was performed using a solution of perchloric acid and ethanol at a voltage of 15 V and −30 °C for 15 s. The crystal structures of the samples were determined by X-ray diffraction (XRD, Bruker D8) at 40 kV and 30 mA using a rotating Cu Kα X-ray source. The scan range was 20°–90° at a scanning speed of 0.5°/min. Tensile testing was performed using a universal tensile testing machine (Shimazu, AGX-10kNX) under tensile strain rates of 3.33×10^{-4}/s. Each alloy was tested three times to ensure consistency of the results.

2.3. Electrochemical measurements

Electrochemical measurements were performed using an electrochemical workstation (Zahner, Zennium) equipped with a three-electrode electrolyte cell. A platinum foil served as the counter electrode and an Ag/AgCl electrode (saturated KCl) was employed as the reference. The test specimens were sealed in epoxy resin to serve as working electrodes. The samples were subsequently immersed in 500 mL of Hanks' solution. Electrochemical impedance spectroscopy (EIS) measurements were performed with a sinusoidal potential of 5 mV amplitude at the open-circuit potential (OCP), sweeping the frequency range from 100 kHz to 10 mHz. EIS spectra were recorded at various intervals (30 min, 1 d, 3 d, 7 d, 14 d, and 30 d), and the data were curve-fitted using Z-Simple software. A potentiodynamic polarization curve was tested at a scanning rate of 1 mV s^{-1} from −2.2 V to −1.1 V versus the reference electrode, following immersion in Hanks' solution for 60 min. All electrochemical tests were performed in duplicate to ensure repeatability of the results.

2.4. In vitro degradation

The *in vitro* degradation rate of the samples was assessed to conduct initial screening through an immersion test in Hanks' solution conducted over a period of 30 d at room temperature. The corrosion rate was determined using the hydrogen collection method [44]. The electrolyte volume in the container was maintained at 500 mL and the evolved hydrogen was continuously collected. The mass loss of the samples was quantified in both the pre- and post-immersion tests using an analytical balance. Subsequently, the morphologies and corrosion products were examined using SEM, EDS, and XRD. After a 30-day immersion period, the corrosion products were removed using CrO_3 and $AgNO_3$ solutions for 10 min, ultrasonically cleaned in ethanol, and air-dried. The surface roughness and corrosive depth of the degraded samples after the removal of the corrosion products were estimated using a three-dimensional laser scanning confocal microscope system (Zeiss, LSM900).

2.5. Biocompatibility

2.5.1. Cell culture

Murine calvarial preosteoblasts (MC3T3-E1) purchased from ATCC were used to evaluate the cytocompatibility of the alloys, which had a behavior similar to that of primary calvarial osteoblasts. To better mimic the *in vivo* situation, the incubation intervals were set to 24 h, and soluble degradation products were regularly removed from the circulatory system at the local implantation site.

2.5.2. Cell viability and cytotoxicity evaluation

The evaluation of cell viability and cytotoxicity were conducted utilizing a cell counting kit-8 (CCK-8) assay. The cells were seeded in 96-well plates at a density of 1×10^4 cells/well and cultured for 24 h. Extracts were added to the culture medium, and normal culture medium was used as a negative control. After 24, 48, and 72 h of incubation, 20 μL of the CCK-8 detection reagent was added to each well and incubated for 1 h. Absorbance was subsequently measured at a wavelength of 450 nm using a microplate spectrophotometer (Thermo Scientific).

The live/dead cell assay was performed according to the protocol of the BestBio manufacturer. Briefly, the cells were stained for 30 min with a 1:10000 diluted calcein-AM solution and 5 min with a 1:5000 dilution of PI solution. Viable cells stained green with calcein-AM, while dead cells stained red with PI, were visualized using fluorescence microscopy (Leica, SP8).

2.5.3. Cell adhesion and morphology

Confocal laser scanning microscopy (CLSM) was used to observe the adhesion and morphology of the actin cytoskeleton in cells co-cultured with the samples after 24, 48, and 72 h. The cells were then washed with PBS, fixed with 4 % paraformaldehyde, and permeabilized with 0.1 % Triton X-100. The nuclei were stained using 4',6-diamidino-2-phenylindole dilactate, while F-actin was stained with Actin-Tracker Green. Cellular imaging was performed using a CLSM system to capture images of the cells on the glass substrate and the sample surface. Additionally, the spread of cells on the sample was investigated using SEM. The SEM procedure involved the immersion of the samples in 2.5 % glutaraldehyde, dehydration with graded ethanol, and tertiary butanol. Finally, the morphologies of the attached cells were observed using SEM.

2.5.4. In vitro degradation of the alloys in DMEM

In vitro degradation of the alloys was assessed by measuring the pH of the collected media after 24, 48, and 72 h of culture.

2.5.5. Quantitative real-time polymerase chain reaction assay

BMSCs were cocultured with small disks of control, BM, FSP-300, and FSP-800, each with a thicknesses of 0.5 cm and diameters of 3 cm in a 6-well plate. DMEM-F12 was added to the cultured BMSCs, and the expression of cell attachment-related genes (integrins α1 and β1) was assessed. The initial detection time was set to 1 d after co-culture with the samples.

RNA was extracted at each time point by using a total RNA kit (Omega Bio-Tek, Norcross). Complementary DNA was synthesized using a PrimeScript RT Reagent Kit (Takara, Shiga, Japan). SYBR premix Ex Taq reagent (Takara) and a CFX Connect Real-Time PCR Detection System (BioRad) were used for quantitative reverse transcriptase polymerase chain reaction (qRT-PCR) detection. Primer sequences were synthesized by Sangon Biotech Co. Ltd. by Primer Premier software. Glyceraldehyde-3-phosphate dehydrogenase was used as the internal control. The relative expression of the target gene was calculated using the 2−Ct method [45].

2.6. In vivo animal studies

2.6.1. Animal model and experimental process

The Animal Care and Experiment Committee and Animal Ethics Committee of the First Affiliated Hospital of Chongqing Medical University (No. 20187801) approved all the animal experiments conducted

in this study. Fifteen 12-week-old Sprague-Dawley (SD) rats were randomly divided into five groups (control, 7d, 15d, 30d, and 60d), with three rats in each group. Prior to the procedure, all rats were anesthetized with an intraperitoneal injection of pentobarbital sodium (30 mg/kg). Four longitudinal incisions parallel to the spine were made on both sides of the back of the rats. A sample of size 5 mm × 5 mm × 1 mm was implanted into a subcutaneous pocket through one of the incisions. The control group underwent only skin incision and did not have any specimens implanted.

The *in vivo* degradation samples were analyzed using high-solution three-dimensional (3D) X-ray computed tomography (Zeiss, Xradia620 Versa). The voltage and power were set to 90 kV and 10 W, respectively. Each scan produced approximately 998 tomographic images with a pixel size of approximately 6 μm at an exposure time of 1 s. The 3D reconstruction of the tomographic images was visualized using the AmiraAvizo3D software. This study focused on 3D rendering and segmentation of the material matrix, corrosion pits, and corrosion products to assess the overall degradability of the implanted materials. Segmentation was performed by distinguishing the grayscale values of different materials, and small noises were removed to ensure result accuracy [46].

2.6.2. Blood testing

Blood samples were collected from each rat before implantation and at 3, 7, 15, 30, and 60 d after implantation, with a volume of 1 mL per collection. Hematological parameters, such as alanine aminotransferase (ALAT), aspartate aminotransferase (ASAT), creatinine (CREA), and serum magnesium ion concentration, were measured using an IDEXX Catalyst One hematological autoanalyzer.

2.6.3. Histological evaluations postsurgery

On days 7, 15, 30, and 60 of implantation, the rats were euthanized, and subcutaneous tissues containing the samples along with vital organs (such as liver, heart, and kidney) were harvested. Harvested tissues were fixed in 4 % paraformaldehyde, dehydrated, and embedded in paraffin. Histological sections were prepared and stained with hematoxylin-eosin (H&E) for general tissue morphology assessment. In addition, immunohistochemical staining was performed using specific antibodies (CD206 and CD86). A chromic acid solution (200 g of CrO_3 and 10 g of $AgNO_3$) was used to clean the samples. The surface morphology was characterized using an optical camera.

2.7. Statistical analyses

Continuous data were expressed as mean ± standard deviation. To

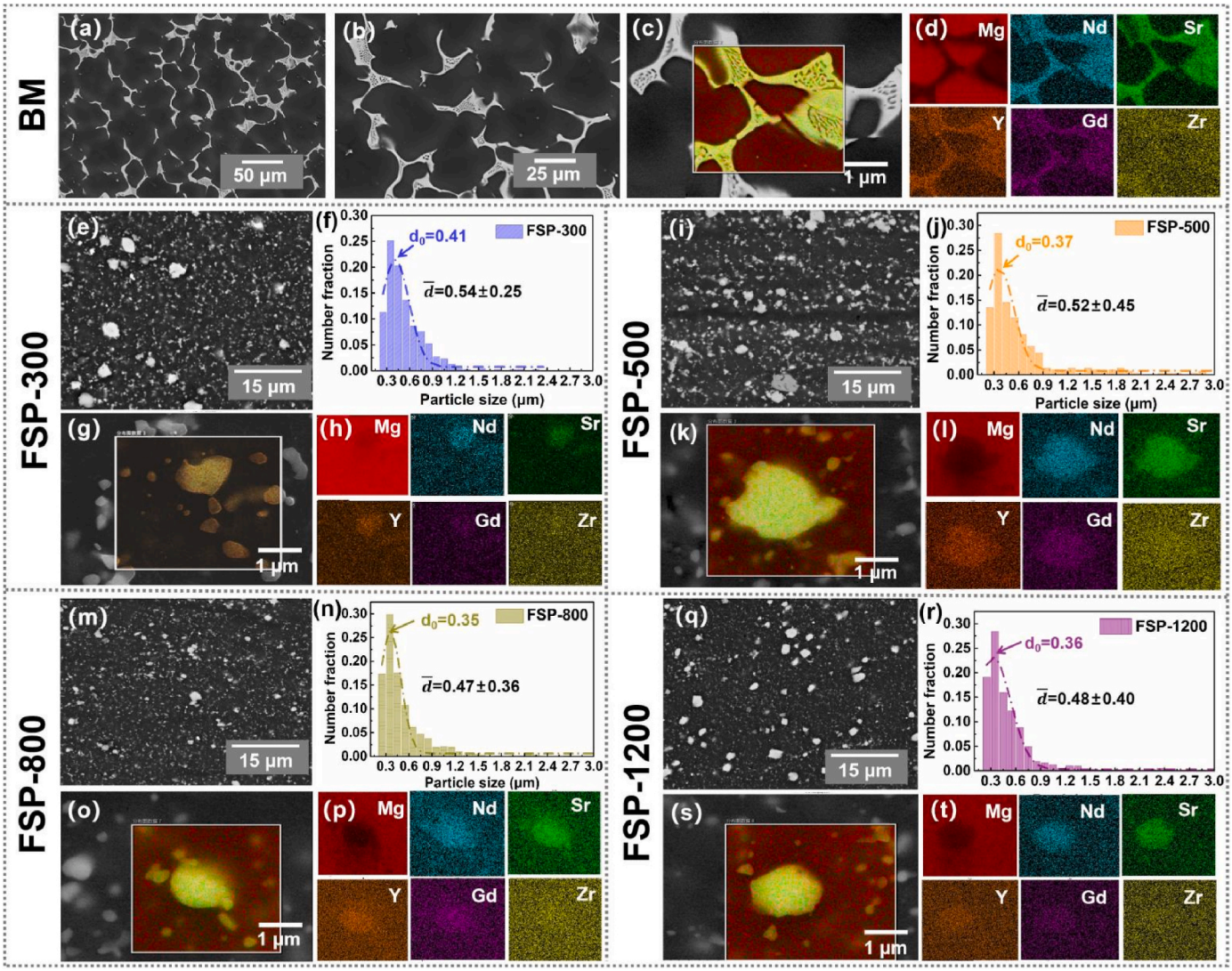

Fig. 1. SEM and elemental mapping images of (a–d) BM, (e, g, h) FSP-300, (i, k, l) FSP-500, (m, o, p) FSP-800, and (q, s, t) FSP-1200. Precipitated phase distributions of (f) FSP-300, (j) FSP-500, (n) FSP-800, and (r) FSP-1200.

determine the statistical significance of different groups, a single-factor one-way analysis of variance (ANOVA) with a post-hoc test was used. A p-value less than 0.05 was considered to be statistically significant. All statistical analyses were conducted using the SPSS software.

3. Results

3.1. Surface morphology, microstructure, and chemical composition

Fig. 1 illustrates the microstructure and chemical composition of WEJ431 alloys before and after FSP. As shown in Fig. 1a, the BM sample exhibited coarse and dendritic precipitated phases that were randomly distributed in the α-Mg matrix. These phases primarily consisted of Y, Nd, Gd, Zr, and Sr (Fig. 1c and d). The presence of Y-rich and Nd-rich particles in the BM was confirmed by EDS analysis (Fig. S3). Combining the XRD spectra shown in Fig. 2a, the two precipitated phases are referred to as the $Mg_{24}Y_5$ and $Mg_{41}Nd_5$ precipitates. These rare-earth elements (Y, Nd, and Gd) were also soluted in the precipitates (Fig. 1c). As shown in Fig. S3, Y element was partially soluted in the α-Mg matrix, but few Nd and Gd elements could be identified in the matrix. The Y content near the precipitates was higher than that in the α-Mg matrix phase far from the precipitates. In addition, most Sr element was detected in the precipitated phases, indicating that Sr was soluted in the precipitates. Zr element was evenly distributed throughout the material. After FSP, refined grains and uniformly distributed precipitates can be observed in Fig. 1e–t and Figs. S2a–d. Notably, at low heat input (rotation speeds of 300 and 500 rpm), most of the coarse precipitated phases were replaced by finer equiaxed spherical particles smaller than 100 nm in size. However, some micron-sized particles were still observed on the surface (Fig. 1e and i). The FSP-800 sample exhibited the finest and most uniformly distributed precipitated phases (compared with Fig. 1e–i, and q). With further increases in the rotation rate, the size of the precipitated phases increased slightly owing to the increase in the heat input. According to the XRD results, the shift in the α-Mg phase suggests the formation of a Y-saturated Mg phase during FSP [47] (Fig. 2b). Among them, the FSP-800 exhibited a higher solid solution content of alloying elements after thermal-mechanical processing.

EBSD analysis of the alloys, both before and after FSP, was conducted on a longitudinal section parallel to the PD. Inverse pole figure (IPF) maps of the samples under different conditions are shown in Fig. 3. All the samples exhibited fully recrystallized and equiaxed grains. The average grain sizes of the BM were 53.2 μm, which were dramatically refined to 2.6 μm in FSP-300, 2.7 μm in FSP-500, 3.4 μm in FSP-800, and 6.1 μm in FSP-1200. The grain sizes significantly decreased after the FSP. Meanwhile, the grain sizes increased marginally but still maintained in the same order of magnitude with increasing heat input during FSP. The measured (0001), (10-10), and (11–20) pole figures are shown in Fig. S4, revealing that all WEJ431 alloys before and after FSP exhibited a relatively strong (0001) basal texture, with the texture strength maintained at the same level. The kernel average misorientation (KAM) distribution maps shown in Fig. 4 can be used to qualitatively characterize the density distribution of dislocations and the strain magnitude in different grains. As shown in Fig. 4b, most areas of the FSP-300 sample are blue, and a few areas are green, indicating that the surface of the sample is almost free of dislocations. With a further increase in the tool rotation speed, a high KAM value was observed near the grain boundaries and inside the grains (Fig. 4c–e). The KAM results shown in Fig. 4e indicate that the FSP-1200 sample had a high dislocation density and was more prone to strain concentration.

3.2. Mechanical properties

Fig. 5 shows the mechanical properties of the WEJ431 alloys before and after FSP, including the ultimate tensile strength (UTS), yield strength (YS), and elongation (EL) to failure. The UTS and YS of the BM were only 135.7 MPa and 188.1 MPa, respectively. After FSP, the strength and elongation of the alloys were significantly enhanced. Based on the microstructural results, it can be inferred that grain refinement and precipitation hardening contributed to the strength of the FSP-treated samples, as illustrated in Fig. 1. Meanwhile, the Y element has been proven to provide an obvious solid solution strengthening effect for Mg alloys owing to serious lattice distortion caused by the significant diameter difference between Mg and Y atoms [48,49]. As a result, grain refinement, precipitate strengthening, and solid solution strengthening collectively increased the strength of the FSP-treated WEJ431 alloys. According to the EBSD results shown in Fig. 3, the grain sizes increased with increasing tool rotation. The tensile strength of the alloys increased with increasing tool rotation speed, as shown in Fig. 5. When the rotation speed was increased to 1200 rpm, the YS and UTS improved to 190.5 MPa and 267.6 MPa, respectively. EI reached its maximum value (8.0 %) at a rotation speed of 800 rpm and then decreased to 6.4 % at a rotation speed of 1200 rpm. Among these samples, FSP-800 exhibited a higher solid solution content of Y element after FSP. Meanwhile, the peak offset in the α-Mg phase for the FSP-1200 sample showed a certain right shift compared with that of the FSP-800 sample. This indicates that a large number of fine precipitates gradually precipitated from the soluted matrix during the cooling of the FSP process at higher input conditions. During the process of tensile deformation, these fine precipitates can effectively pin dislocations and grain boundary movement, substantially enhancing the precipitation strengthening in the FSP-1200 sample. As reported in Ref. [50], grain refinement would improve the plasticity by enhancing the homogeneity of plastic deformation in the metallic materials with a strong basal texture. Thus, the elongation after FSP was increased by the grain refinement compared to the BM sample, as depicted in Fig. 3. However, the precipitates in FSP-1200 may pin dislocations or hindered their movement, thereby reducing the elongation with increasing the tool rotation speed to 1200 rpm [51,52].

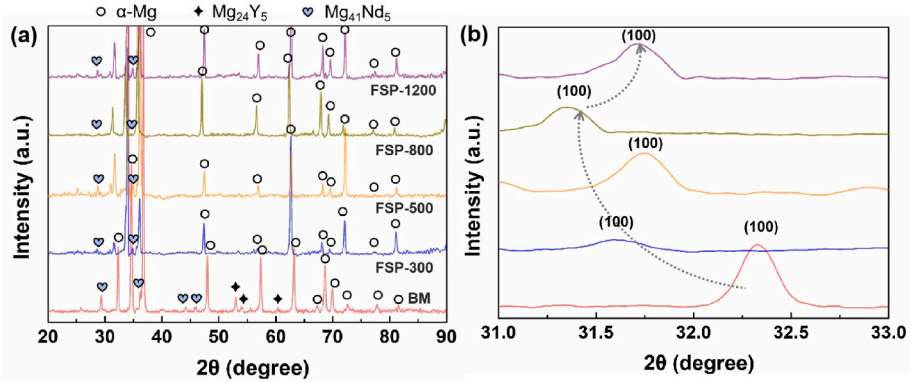

Fig. 2. (a) XRD patterns of BM, FSP-300, FSP-500, FSP-800, and FSP-1200. (b) Detailed XRD patterns from 31° to 33°.

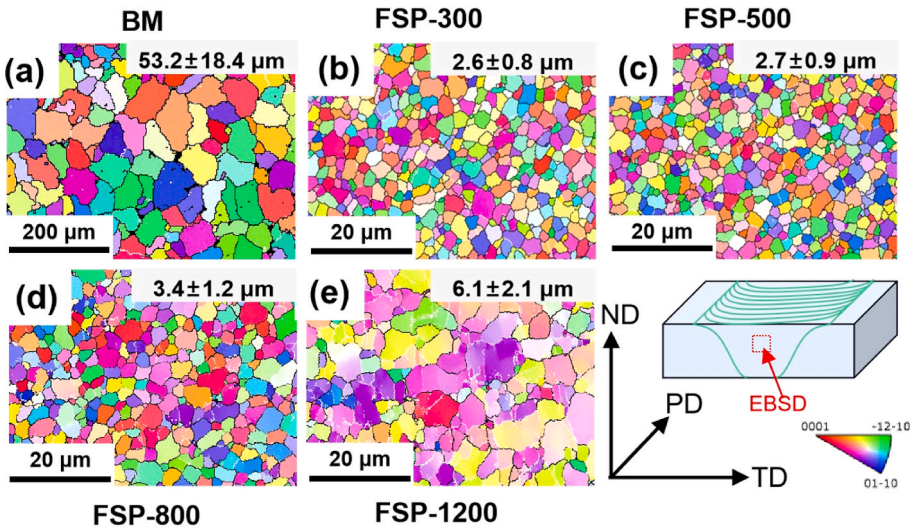

Fig. 3. Inverse pole figure (IPF) maps and average grain sizes of (a) BM, (b) FSP-300, (c) FSP-500, (d) FSP-800, and (e) FSP-1200.

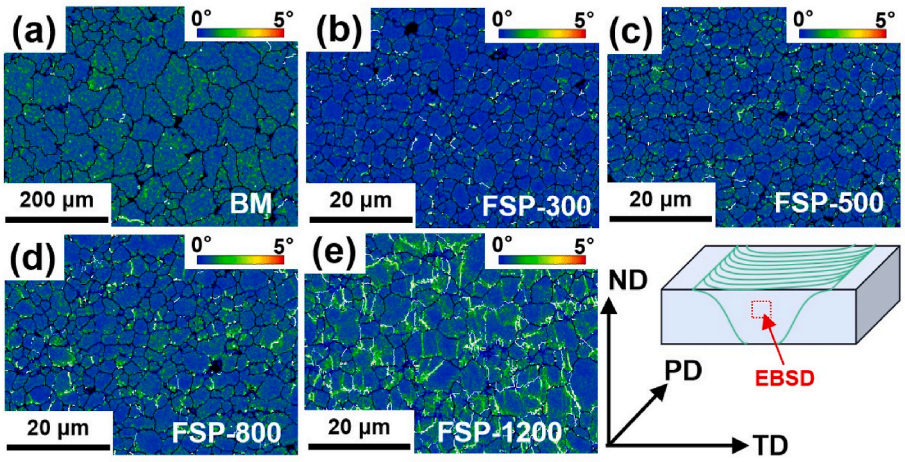

Fig. 4. Kernel average misorientation (KAM) distribution maps of (a) BM, (b) FSP-300, (c) FSP-500, (d) FSP-800, and (e) FSP-1200. KAM values are indicated by color bands ranging from 0° (minimum) to 5° (maximum).

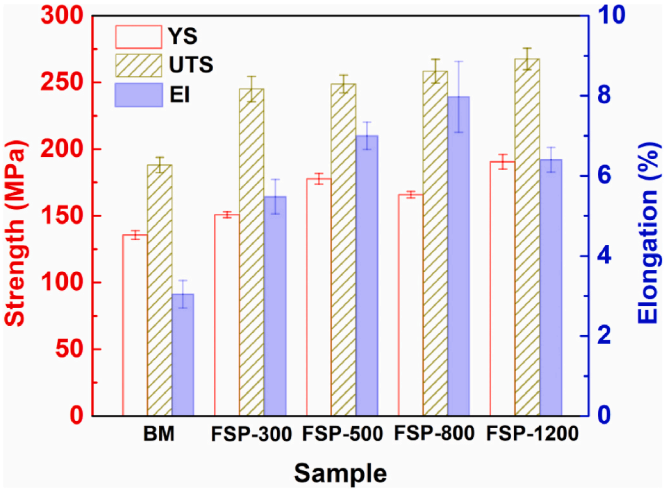

Fig. 5. Tensile mechanical properties of BM, FSP-300, FSP-500, FSP-800, and FSP-1200.

3.3. *In vitro* degradation

3.3.1. *Electrochemical impedance spectroscopy*

EIS tests were performed to evaluate the *in vitro* degradation of the samples. After immersion in Hanks' solution for 7 d, the BM sample collapsed and shattered, making it challenging to continuously monitor stable EIS data. The impedance modulus of BM decreased sharply during the immersion period (Fig. 6a). For the FSP-treated samples, EIS remained stable during the 30-day immersion period. In addition, the alloys exhibited different corrosion behaviors during the immersion period. Specifically, in the Bode plots of the BM, FSP-300, FSP-500, and FSP-1200 samples, a plateau that changed to a positive slope in the low-frequency range corresponded to the inductance of the Mg alloys. This was related to the unstable dissolution of the surface film. The inductance can be regarded as a pseudo-element that represents the self-catalytic electrochemical processes. The equivalent circuit of Model A in Fig. 7a was used to fit the EIS results of the samples. However, the FSP-800 sample in the initial period did not show inductance characteristics. Hence, the local autocatalytic reaction was negligible. The model B equivalent circuit in Fig. 7a was applied to fit the EIS results of the FSP-800 sample in the first 3 d, which was similar to the model for a surface-coated Mg alloy [53]. The EIS corrosion process of FSP-800

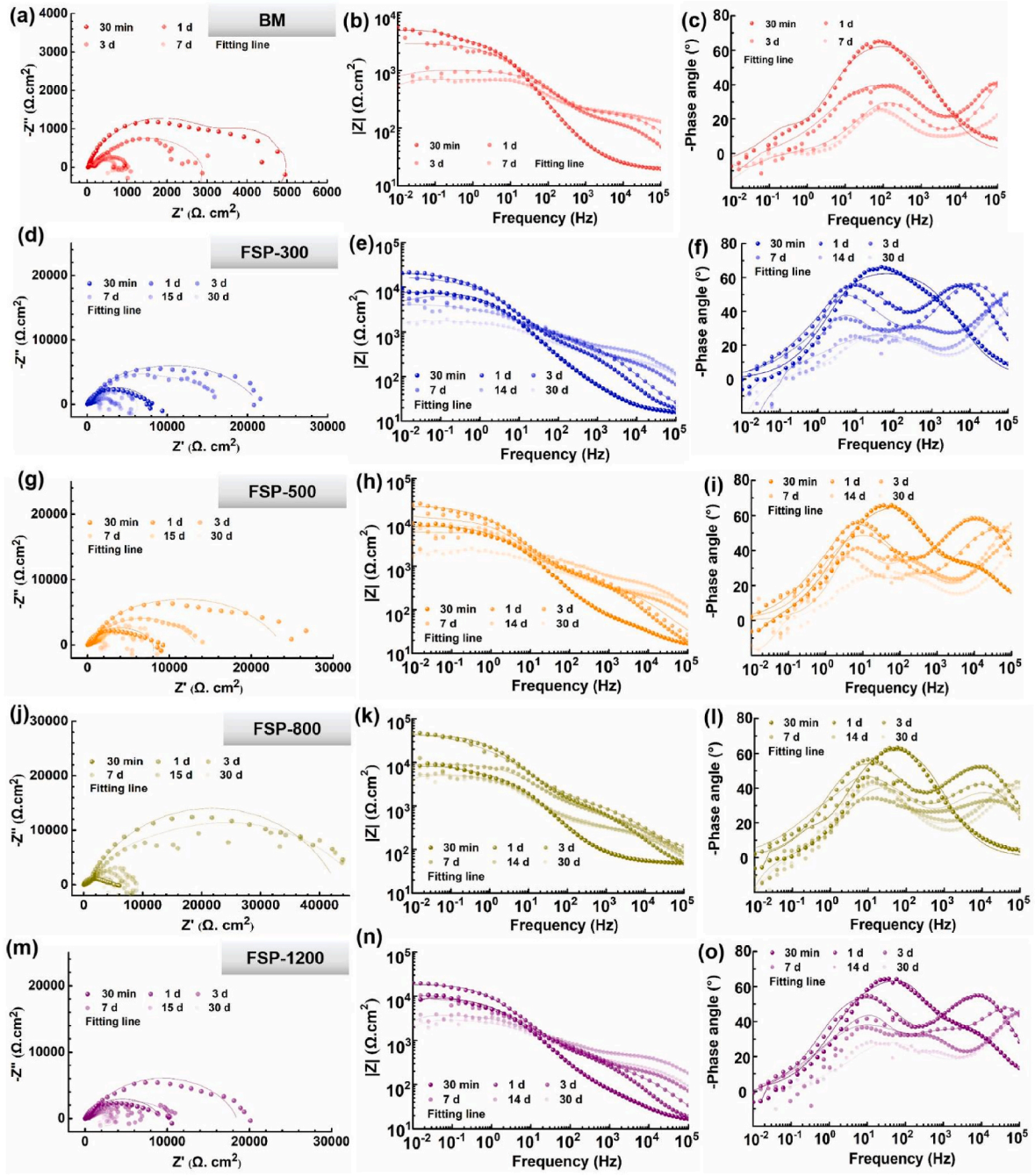

Fig. 6. Typical Nyquist and Bode plots for (a–c) BM, (d–f) FSP-300, (g–i) FSP-500, (j–l) FSP-800, and (m–o) FSP-1200 after immersion in Hanks' solution for different durations.

suggested local breakdown of the surface film and exposure of the alloy substrate, which was fitted by equivalent circuit A. In these circuits, R_s represents the solution resistance, CPE_f represents the constant phase element, R_f is the surface film resistance, and R_{ct} and CPE_{dl} are the charge transfer resistance and double-layer capacitance, respectively. R_L and L correspond to resistance and inductance, respectively. The fitting electrochemical parameters of the samples are presented in Tables 2–6. In this study, the capacitance of the surface film C_f was calculated from the fitted CPE_f based on Equation (1) [1]:

$$C_f = {Y_0}^{1/n} {R_f}^{(1-n)/n} \tag{1}$$

where Y_0 and n are the admittance of a non-ideal capacitor and an empirical constant ranging from 0 to 1, respectively, and R_f is the surface film resistance. The capacitance of the double layer (C_{dl}) was calculated using Equation (2) [1]:

$$C_{dl} = {Y_{dl}}^{1/n} \left(\frac{1}{R_s} + \frac{1}{R_{ct}} \right)^{(n-1)/n} \tag{2}$$

where Y_{dl} represents the admittance of the double layer, and R_f and R_{ct} are the surface film and charge transfer resistances, respectively.

According to the circuit, the polarization resistance (R_p), which is proportional to the corrosion rate, can be calculated using Equation (3):

$$R_p = R_f + \frac{R_{ct} R_L}{R_{ct} + R_L} \quad (\text{Model A}) \tag{3}$$

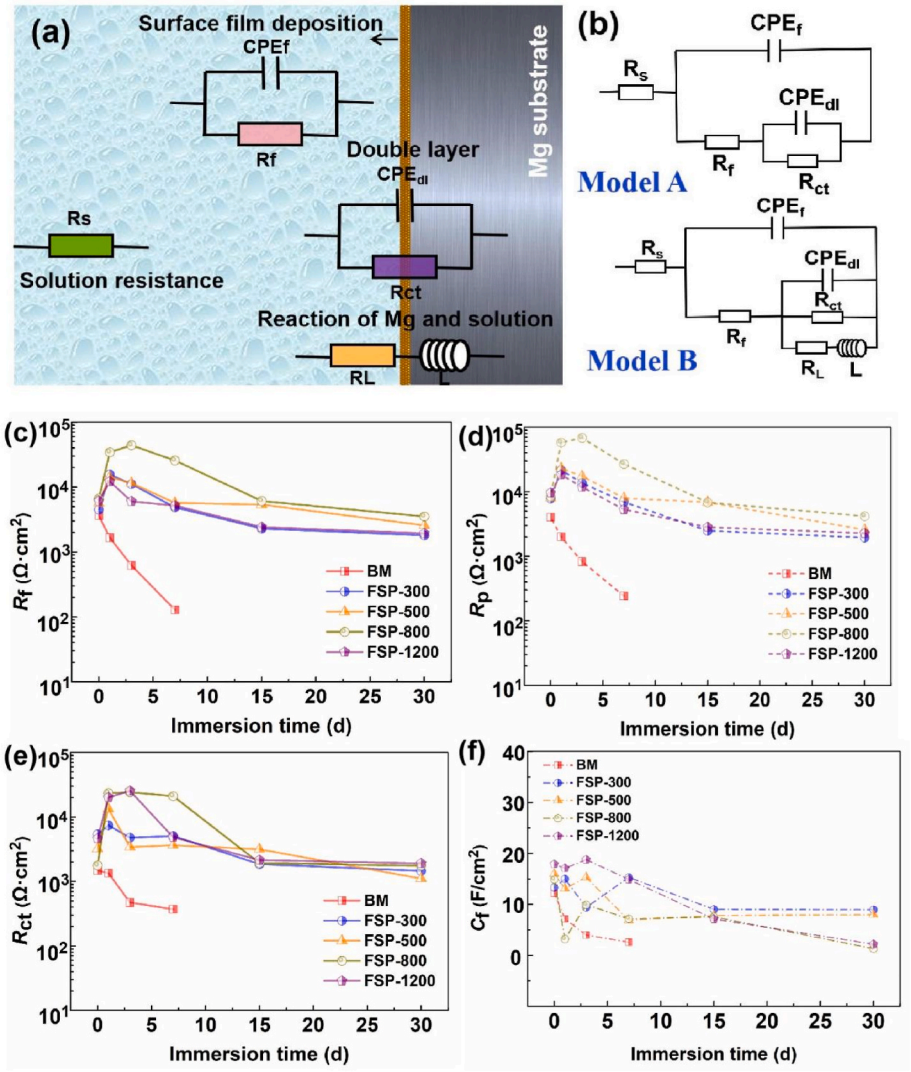

Fig. 7. (a, b) Equivalent circuit models for EIS results of BM, FSP-300, FSP-500, FSP-800, and FSP-1200 samples at different immersion periods. (c) Film resistance (R_f), (d) calculated polarization resistance (R_p), (e) charge transfer resistance (R_{ct}) and (f) capacitance of the surface film (C_f) of these samples in Hanks' solution.

Table 2
Fitting EIS parameters of BM.

Immersion time (d)	R_s (Ω·cm^2)	C_f (F/cm^2)	R_f (Ω·cm^2)	C_{dl} (F/cm^2)	R_{ct} (Ω·cm^2)	R_L (Ω·cm^2)	L (H/cm^2)	R_p (Ω·cm^2)
0	20.73	1.22×10^{-5}	3.64×10^{3}	3.77×10^{-4}	1.48×10^{3}	5.48×10^{2}	4.98×10^{4}	4.04×10^{3}
1	19.13	7.18×10^{-6}	1.67×10^{3}	1.69×10^{-5}	1.35×10^{3}	4.35×10^{2}	4.43×10^{4}	2.00×10^{3}
3	15.47	3.97×10^{-6}	6.23×10^{2}	1.18×10^{-3}	4.72×10^{2}	3.65×10^{2}	2.31×10^{3}	8.29×10^{2}
7	19.34	2.59×10^{-5}	1.29×10^{2}	1.41×10^{-5}	3.71×10^{2}	1.66×10^{2}	2.37×10^{3}	2.43×10^{2}

Table 3
Fitting EIS parameters of FSP-300.

Immersion time (d)	R_s (Ω·cm^2)	C_f (F/cm^2)	R_f (Ω·cm^2)	C_{dl} (F/cm^2)	R_{ct} (Ω·cm^2)	R_L (Ω·cm^2)	L (H/cm^2)	R_p (Ω·cm^2)
0	16.13	1.33×10^{-5}	4.52×10^{3}	1.41×10^{-5}	5.38×10^{3}	8.75×10^{3}	4.86×10^{2}	7.85×10^{3}
1	14.52	1.50×10^{-5}	1.56×10^{4}	4.52×10^{-6}	7.42×10^{3}	3.24×10^{4}	7.43×10^{3}	2.16×10^{4}
3	19.20	9.39×10^{-6}	1.11×10^{4}	1.30×10^{-5}	4.79×10^{3}	5.23×10^{3}	2.21×10^{3}	1.36×10^{4}
7	14.21	1.53×10^{-5}	4.89×10^{3}	2.90×10^{-5}	5.08×10^{3}	3.47×10^{3}	4.22×10^{3}	6.95×10^{3}
15	22.99	9.01×10^{-6}	2.30×10^{3}	8.31×10^{-6}	1.86×10^{3}	2.12×10^{2}	5.94×10^{3}	2.49×10^{3}
30	20.51	8.96×10^{-6}	1.81×10^{3}	3.73×10^{-4}	1.46×10^{3}	1.54×10^{2}	6.73×10^{2}	1.95×10^{3}

$$R_p = R_f + R_{ct} \quad \text{(Model B)} \tag{4}$$

The R_f and calculated R_p values of these samples are summarized in Fig. 7c and d. R_p serves as an indicator to evaluate the corrosion properties of the materials. According to the results in Fig. 7d, the R_p values of the FSP-treated samples were higher than those of the BM throughout

Table 4
Fitting EIS parameters of FSP-500.

Immersion time (d)	R_s (Ω·cm^2)	C_f (F/cm^2)	R_f (Ω·cm^2)	C_{dl} (F/cm^2)	R_{ct} (Ω·cm^2)	R_L (Ω·cm^2)	L (H/cm^2)	R_p (Ω·cm^2)
0	18.84	1.60×10^{-5}	5.63×10^{3}	5.44×10^{-6}	3.21×10^{3}	8.83×10^{3}	7.42×10^{3}	7.98×10^{3}
1	17.68	1.31×10^{-5}	1.43×10^{4}	5.41×10^{-6}	1.34×10^{4}	1.02×10^{4}	1.04×10^{3}	2.31×10^{4}
3	21.66	1.53×10^{-5}	1.15×10^{4}	2.98×10^{-6}	3.42×10^{3}	4.38×10^{3}	1.16×10^{3}	1.74×10^{4}
7	16.74	6.88×10^{-6}	5.71×10^{3}	4.50×10^{-6}	3.65×10^{3}	5.75×10^{3}	4.52×10^{3}	7.94×10^{3}
15	18.27	7.82×10^{-6}	5.40×10^{3}	1.37×10^{-5}	3.16×10^{3}	2.83×10^{3}	2.10×10^{3}	6.89×10^{3}
30	22.85	7.99×10^{-6}	2.21×10^{3}	3.64×10^{-5}	1.11×10^{3}	5.39×10^{2}	1.22×10^{3}	2.57×10^{3}

Table 5
Fitting EIS parameters of FSP-800.

Immersion time (d)	R_s (Ω·cm^2)	C_f (F/cm^2)	R_f (Ω·cm^2)	C_{dl} (F/cm^2)	R_{ct} (Ω·cm^2)	R_L (Ω·cm^2)	L (H/cm^2)	R_p (Ω·cm^2)
0	20.39	1.49×10^{-5}	6.66×10^{3}	4.18×10^{-4}	1.78×10^{3}	–	–	8.44×10^{3}
1	16.83	3.19×10^{-6}	3.43×10^{4}	5.20×10^{-6}	2.34×10^{4}	–	–	5.77×10^{4}
3	19.32	9.93×10^{-6}	4.41×10^{4}	1.22×10^{-6}	2.43×10^{4}	–	–	6.84×10^{4}
7	23.04	7.18×10^{-6}	2.57×10^{4}	5.04×10^{-6}	2.10×10^{4}	1.24×10^{3}	2.11×10^{3}	2.69×10^{4}
15	24.40	7.56×10^{-6}	6.12×10^{3}	3.39×10^{-6}	1.93×10^{3}	1.15×10^{3}	1.64×10^{4}	6.84×10^{3}
30	21.74	1.31×10^{-6}	3.50×10^{3}	5.17×10^{-6}	1.82×10^{3}	1.11×10^{3}	2.67×10^{4}	4.19×10^{3}

Table 6
Fitting EIS parameters of FSP-1200.

Immersion time (d)	R_s (Ω·cm^2)	C_f (F/cm^2)	R_f (Ω·cm^2)	C_{dl} (F/cm^2)	R_{ct} (Ω·cm^2)	R_L (Ω·cm^2)	L (H/cm^2)	R_p (Ω·cm^2)
0	17.22	1.79×10^{-5}	6.12×10^{3}	2.37×10^{-5}	4.65×10^{3}	1.38×10^{4}	1.23×10^{3}	9.59×10^{3}
1	21.89	1.71×10^{-5}	1.22×10^{4}	5.46×10^{-6}	2.01×10^{4}	8.71×10^{3}	1.68×10^{3}	1.83×10^{4}
3	16.71	1.88×10^{-5}	6.02×10^{3}	2.01×10^{-6}	2.54×10^{4}	7.48×10^{3}	8.86×10^{2}	1.18×10^{4}
7	14.17	1.49×10^{-5}	5.21×10^{3}	2.30×10^{-6}	4.86×10^{3}	1.12×10^{2}	1.42×10^{3}	5.32×10^{3}
15	16.23	4.57×10^{-5}	2.42×10^{3}	1.13×10^{-5}	2.15×10^{3}	4.89×10^{2}	3.43×10^{4}	2.82×10^{3}
30	22.58	2.18×10^{-6}	1.94×10^{3}	8.76×10^{-6}	1.91×10^{3}	4.20×10^{2}	3.07×10^{4}	2.28×10^{2}

the immersion period, indicating superior corrosion resistance. Concurrently, the R_p values of the BM sharply decreased during the 7-day immersion period, suggesting that the sample experienced severe corrosive erosion. As shown in Fig. 7c and Tables 2, 3, 4, 5 and 6, the R_f values of the alloys after FSP were larger than those of the BM, implying a more protective film deposited on the surface of the FSP-treated alloys. Moreover, the R_f and R_p values of the FSP-treated samples slightly increased during the initial immersion stage, decreased after 7 d of immersion, and then remained stable at a high level throughout the entire immersion process. This indicates that the alloys after FSP can achieve long-term stability of the surface film and more stable corrosion resistance. Similarly, the C_f values are also related to the properties of the surface films on alloys [54]. The C_f values of the FSP-treated samples remained relatively stable during degradation. Among these FSP-treated

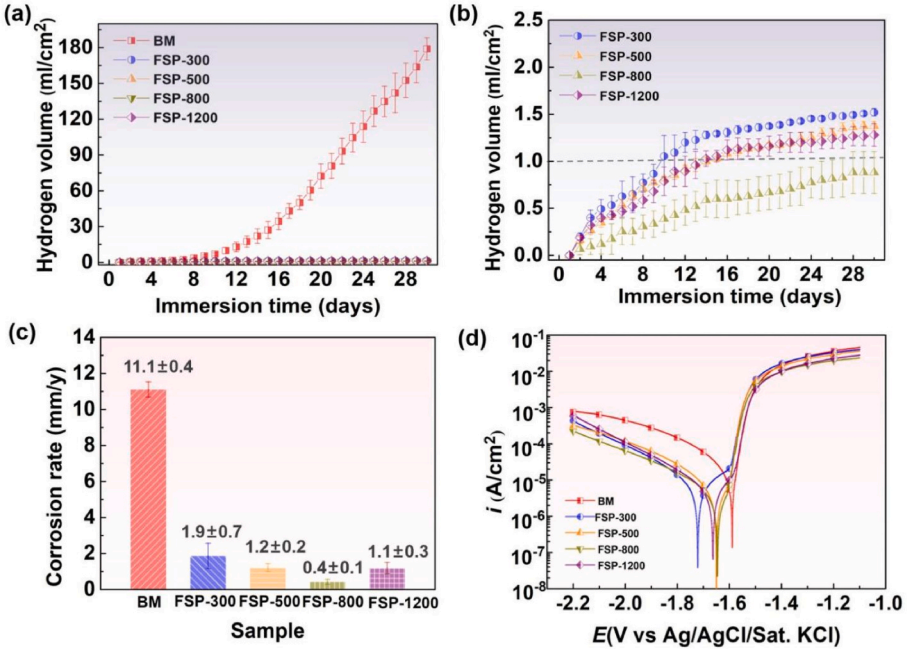

Fig. 8. (a, b) Hydrogen evolution volumes and (c) corrosion rates of BM, FSP-300, FSP-500, FSP-800, and FSP-1200 in Hanks' solution for 30 d. (d) Potentiodynamic polarization curves of BM, FSP-300, FSP-500, FSP-800, and FSP-1200 in Hanks' solution.

samples, the C_f values of the FSP-800 sample were relatively small, which indicates that the surface film on this sample was smoother and denser, thereby inhibiting electrochemical corrosion reactions between the substrate and solution [53]. Moreover, R_f, R_{ct}, and R_p of the FSP-800 sample were relatively higher than those of the other samples during the degradation period, indicating the significantly enhanced corrosion protection of this sample.

3.3.2. Hydrogen evolution test

Hydrogen evolution is a crucial factor in evaluating biodegradable Mg alloys because it can help intuitively predict the production of hydrogen during *in vivo* biodegradation. Fig. 8a and b displays the hydrogen (H_2) evolution of the BM, FSP-300, FSP-500, FSP-800, and FSP-1200 samples in Hanks' solution. As expected, BM exhibited the highest H_2 evolution volume and fastest H_2 evolution rate (Fig. 8a). The amount of H_2 accumulated over time and the H_2 evolution rate of the BM increased slowly in the early stage and then accelerated sharply after immersion for 7 d. This implies that for the casting sample, once the surface underwent uneven corrosion, the corrosion rate significantly increased, eventually leading to severe damage to the sample [53,55]. As shown in Fig. 8a and b, the amount of H_2 in the alloys after FSP decreased significantly compared to that in the as-cast alloy, while the order of the H_2 amount for the FSPed alloys was FSP-300 > FSP-500 > FSP-1200 > FSP-800. Interestingly, the total hydrogen evolution of FSP-800 was lower than 1 mL/cm^2 after 30 d of degradation in Hanks' solution. The corrosion rate calculated based on the mass loss was consistent with that of the hydrogen evolution. The corrosion rate of the alloys after FSP significantly decreased by 82.9%–93.9 % compared to that of the BM. Moreover, the FSP-800 sample exhibited the best corrosion resistance with an *in vitro* corrosion rate of only 0.4 mm/y.

Fig. 8d presents the potentiodynamic polarization curves of the BM, FSP-300, FSP-500, FSP-800, and FSP-1200 samples after immersion in Hanks' solution for 60 min. The corresponding corrosion potential (E_{corr}) and corrosion current density (i_{corr}) estimated from the polarization curves are listed in Table 7. BM exhibited the highest i_{corr}, whereas the alloys after the FSP treatment had a lower i_{corr}. For the BM sample, a sudden increase in current was observed in the anodic polarization curve. This suggests that the surface film formed during the corrosion process had a minimal protective effect, leading to the rapid dissolution of Mg alloys. Notably, both samples after FSP treatment exhibited a slight pseudo-passive region on their anodic polarization curves, which can be attributed to the formation of a protective film in Hanks' solution. The subsequent rapid increase in the current corresponded to the breakdown of the surface films. The breakdown potential of the FSP-800 sample was relatively positive, indicating greater protectiveness of the surface film. Additionally, the FSP-800 sample had the lowest corrosion current density among these samples (i_{corr} = 3.38 μA/cm^2).

3.3.3. Corrosion morphology and product analysis

Fig. 9 depicts the typical corrosion surface morphology evolution with constituents of corrosion products on the BM- and FSP-treated alloys after immersion in Hanks' solution for varying periods of time. As shown in Fig. 9a, the BM exhibited numerous loose corrosion products and a rough surface after immersion for 7 d. With the extension of the immersion time, the corrosion of the BM gradually intensified, and the corrosion products accumulated quickly (Fig. 9f). When the immersion time reached 30 d, large amounts of corrosion products were deposited on the cracked corrosion surface, which were composed of Mg, O, C, Ca, P, and a small amount of rare earth elements, according to the EDS results in Fig. 9p. Deep corrosion pits appeared on the surface of the BM, indicating severe damage to the sample (Fig. 9k). This phenomenon corresponded to the results observed in the polarization curves shown in Fig. 8d. The non-protective effect of the surface film on the BM surface led to rapid dissolution of the Mg alloy in the early corrosion stage, resulting in the formation of some localized corrosion pits. The corrosion surfaces of the Mg alloys after FSP were relatively smooth compared with those of the BM, and there were no obvious large corrosion pits. In addition, more RE elements, including Y, Nd, and Gd, were detected on the corroded surface after the FSP treatment. As depicted in Fig. 9b–g, l, and q, FSP-300 suffered relatively slight corrosion destruction during the entire immersion period, with only a few corrosion product films formed on the surface with a mixture of Mg hydroxides and phosphates. After immersion for 15–30 d, the corrosion products gradually accumulated on the surface of FSP-300 (Fig. 9g and l). The corrosion morphological characteristics of FSP-500 were similar to those of the FSP-300 sample (Fig. 9c–h, m, and r), with the specific performance being the accumulation of corrosion products appearing in the later stage of corrosion. As shown in Fig. 9d–i, n, and s, FSP-800 maintained a smooth surface and a dense surface film deposited without the accumulation of corrosion products after immersion in Hanks' solution. The entire surface suffered more uniform corrosion than that of the other materials. The FSP-1200 sample exhibited a relatively more serious corrosion phenomenon (Fig. 9e–j, o, and t) than the FSP-800 sample. Notably, the slight pseudo-passive region in the anodic polarization curves of the FSPed samples can also reflect the formation of a protective surface film during corrosion.

Table 7
Corrosion potential (E_{corr}) and corrosion current density (i_{corr}) estimated from the polarization curves.

Samples	E_{corr} (V vs Ag/AgCl)	i_{corr} (A/cm^2)
BM	−1.59	3.96×10^{-5}
FSP-300	−1.72	6.92×10^{-6}
FSP-500	−1.65	6.31×10^{-6}
FSP-800	−1.64	3.38×10^{-6}
FSP-1200	−1.66	4.16×10^{-6}

3.4. In vitro biocompatibility

The biocompatibility of representative group of BM, FSP-300 and FSP-800 materials was preliminarily evaluated *in vitro* through co-culturing the materials with bone marrow mesenchymal stem cells (BMSCs). Among them, the BM as the contrast material, FSP-300 and FSP-800 are typical materials with the highest corrosion rate and the lowest corrosion rate after processing, respectively. Live/dead staining was performed to assess the cytotoxicity of the materials visually. The live/dead staining images in Fig. 10 of BMSCs co-cultured with extracts for 72 h indicate the presence of live cells in all groups, with only a few dead cells. The control and FSP-800 groups exhibited diverse live cells that almost filled the entire field, while dead cells were scarce. In contrast, the BM group had significantly more dead cells than the other groups did. These results confirmed the excellent cytocompatibility of the FSP-800 alloy (Fig. 10f).

To further evaluate the effect of the materials on cell proliferation, a CCK-8 assay was performed (Fig. 10e). The results demonstrated good cytocompatibility of both FSP-300 and FSP-800 alloys, with the latter showing the strongest ability to promote cell proliferation, possibly owing to its superior anti-corrosion properties. Moreover, the cytotoxicity of FSP-800 alloys should fall within Grade 0 or Grade 1, according to ISO 10993-5 [56].

The initial adhesion, morphology, and viability of BMSCs were evaluated to explore the *in vitro* cytocompatibility of the samples. Integrins α1 and β1 are crucial for cell adhesion and their gene expression reflects the level of cell adhesion. As demonstrated by the PCR results (Fig. 11f and g), gene expression analysis of integrins α1 and β1 showed that their expression in the BM and FSP-300 groups was significantly lower than that in the control groups. However, the expression of integrins α1 and β1 in the FSP-800 group was closed in the first 3 d and significantly increased at the 7-day time point compared to the control group. In addition, the morphology of BMSCs observed

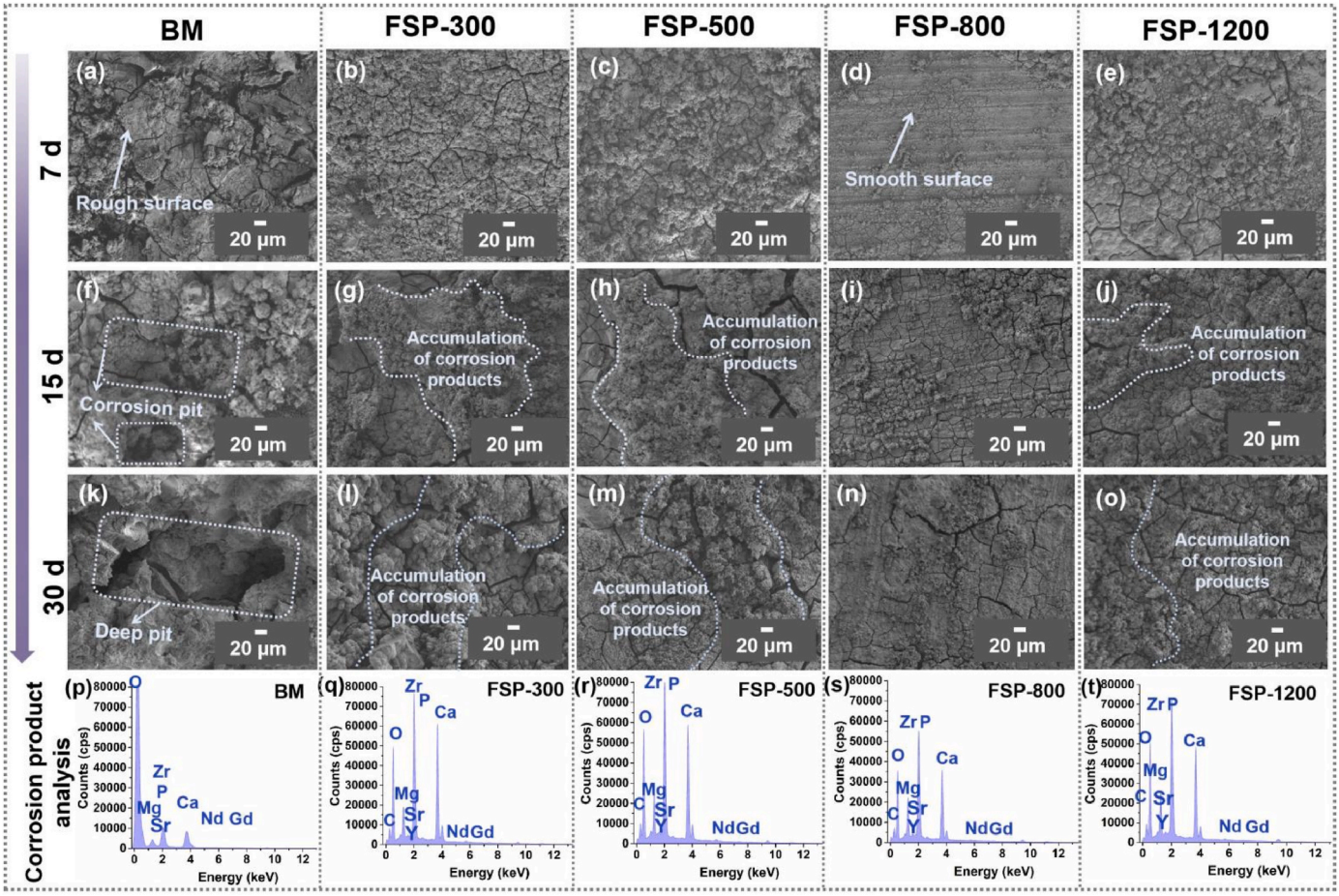

Fig. 9. Surface morphologies and corresponding EDS analysis of (a, f, k, and p) BM, (b, g, l, and q) FSP-300, (c, h, m, and r) FSP-500, (d, i, n, and s) FSP-800, and (e, j, o, and t) FSP-1200 after immersion in Hanks' solution for different periods.

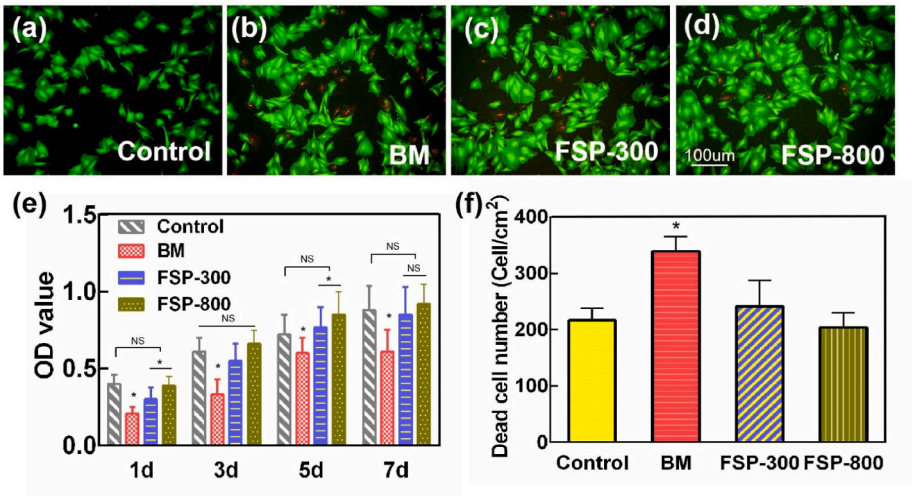

Fig. 10. (a–d) Live/dead staining of BMSCs after co-culture with the control, BM, FSP-300, and FSP-800 extracts. (e) Cell viability of BMSCs evaluated using the CCK-8 assay. (f) Dead cell numbers after co-culture with the control, BM, FSP-300, and FSP-800. Error bars represent mean ± SD for n = 6 (*$p < 0.05$).

through cytoskeleton staining revealed that the cells on FSP-800 exhibited more spreading and pseudopodia than the other groups, indicating enhanced cell attachment and spreading (Fig. 11a–d).

Cell roundness analysis showed that the BM and FSP-300 groups induced cell deformation and death, as evidenced by a significant decrease in cell roundness compared with the control group (Fig. 11a–d). In contrast, the FSP-800 group did not show a significant decrease in cell roundness compared with the control group (Fig. 11e), indicating better biocompatibility. This finding was consistent with the results of live/dead staining.

Overall, the findings suggest that the FSP-800 alloy demonstrated excellent cytocompatibility, promoted cell proliferation, enhanced cell

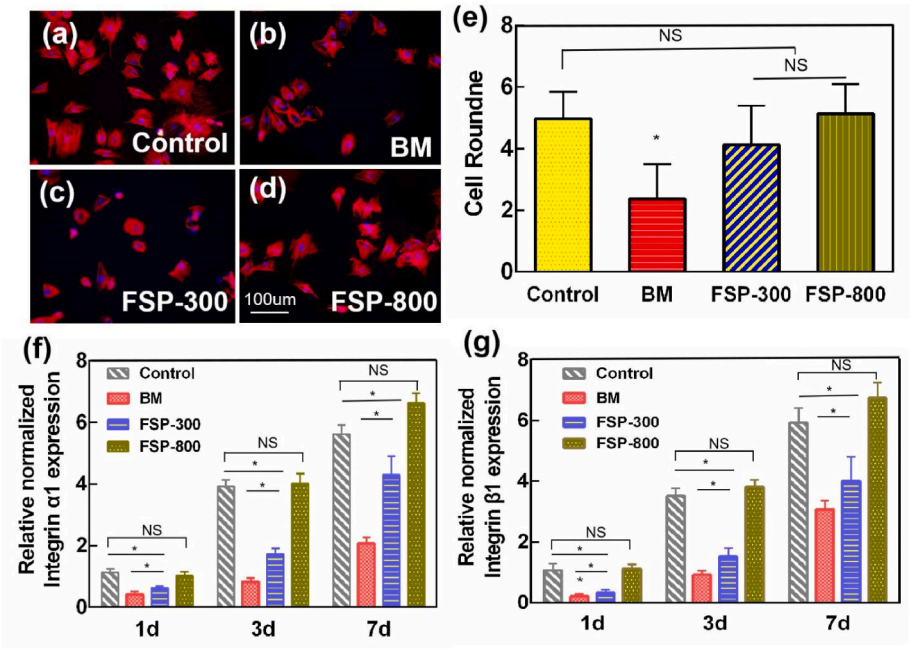

Fig. 11. (a–d) Initial BMSC adhesion and cytoskeleton staining of BMSCs from different groups; (e) calculated roundness of cells. Error bars represent mean ± SD for n = 30 (*$p < 0.05$). Integrins (f) α1 and (g) β1 of BMSCs grown on different substrates after culturing for various periods. β-actin was used as a control. Error bars represent mean ± SD for n = 3 (*$p < 0.05$).

attachment, and maintained cell morphology, indicating its superior biocompatibility compared to the other materials evaluated.

3.5. *In vivo* degradation

The *in vivo* degradation processes of BM, FSP-300, and FSP-800 implants were evaluated based on μCT investigations. Fig. 12a shows the 3D reconstructions of the *in vivo*-degrading implants after different periods. The corresponding digital photographs and screenshots in different directions of the 3D micro-CT images of the *in vivo* degraded implants are shown in Figs. S3 and S4. The BM implants exhibited several surface pits within the first 7 d of degradation, whereas almost no corrosion was observed on the FSP-300 and FSP-800 implants. Meanwhile, some larger corrosion pits were easily observed in the 3D reconstructed BM images after implantation for 14 and 30 d (Fig. 12a). Unfortunately, rapid degradation of the BM implant occurred after 30 d, making it difficult to distinguish the initial shape, and there were numerous permeable corrosion pits on the BM surface. The FSP-300 implants maintained their original morphologies within 14 d of implantation, and slight corrosion traces were detected after being implanted for 30 d after implantation. Notably, almost no corrosion of the FSP-800 implants was observed, which preserved their integrity during the 30-day implantation period. When the degradation time was extended to 60 d, the FSP-800 implants began to degrade slowly, exhibiting 3D morphological characteristics of uniform degradation.

Implant volume loss was analyzed based on μCT measurements, and the *in vivo* corrosion rate (C_r) of these materials was calculated using Equation (5):

$$C_r = \frac{\Delta V}{A \times t} \tag{5}$$

where ΔV represents the implant volume loss (mm^3), and A and t are the surface area (mm^2) and implantation time (year), respectively. The

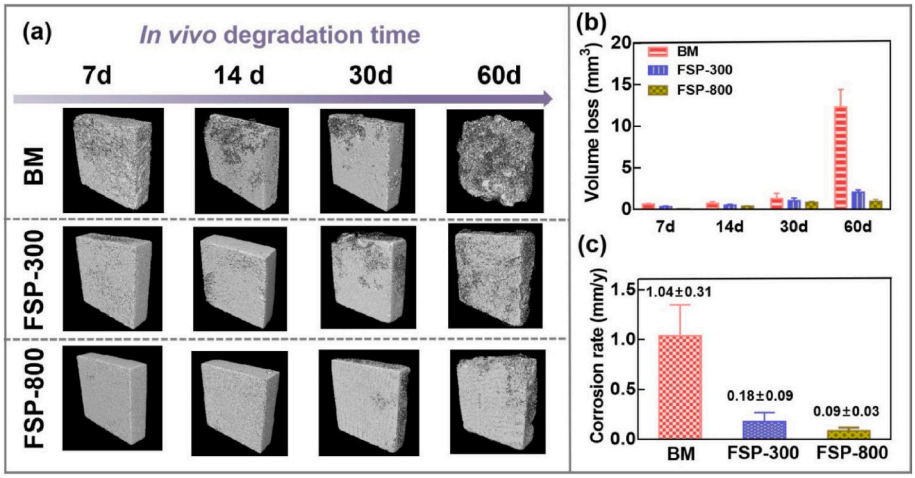

Fig. 12. (a) Representative 3D reconstructions of the implanted BM, FSP-300, and FSP-800 at different time periods. (b) Volume loss at different degradation times and (c) corrosion rate calculated for the samples after degradation for 60 d, as assessed by μCT measurements.

implant volume loss and corresponding *in vivo* corrosion rate are presented in Fig. 10b and c. Regarding the BM implants, the volume loss exhibited a relatively consistent growth rate in the initial 30 d, which then sharply increased with the extension of implantation duration. By the time the degradation period was extended to 60 d, the volume loss of the BM implant reached 12.3 mm^3, and the associated *in vivo* corrosion rate escalated to 1.04 mm/y. The *in vivo* degradation trend mirrored that inferred from *in vitro* weight loss tests. However, the *in vitro* degradation reached the stage of accelerated degradation earlier, and the overall *in vivo* corrosion rate was lower than that of the *in vitro* degradation. For the samples treated with FSP, the implant volume loss slightly increased and remained low throughout the degradation period. Remarkably, the FSP-800 implant achieved an impressively low *in vivo* corrosion rate of approximately 0.09 mm/y. This demonstrates that the processed alloy that we designed has significant potential for orthopaedic clinical applications.

3.6. Biosafety

The biological safety of the materials was comprehensively assessed using a combination of methods including histological sections, blood tests, and immunohistochemistry. The degradation products from the BM, FSP-800, and FSP-300 alloys were monitored as they entered the bloodstream, and the serum biochemical indices associated with liver and kidney functions were closely monitored. The results from Fig. S7a indicated that there were no significant differences in body weight among all SD rats throughout the experimental period, suggesting that the implanted materials did not have a negative impact on the feeding and nutrition of the SD rats. Because implanted materials undergo degradation reactions inside the body, some degradation products enter the circulatory system. By assessing the biological safety through measuring the Mg content in circulation, the results presented in Fig. S5b showed that in the early stage of material implantation (24 h and 7 d), the blood Mg levels were higher in the BM and FSP-300 groups than in the other groups. This correlation was linked to the degradation rate of materials implanted in the body. However, in the later stage of implantation (14 d), because of the stabilization of the degradation rate of the materials and the body's self-regulation, there were no significant differences in blood Mg levels among the groups, confirming the biological safety of the FSP-800 and FSP-300 samples. In addition, histological analysis of the liver, kidneys, and heart of the experimental SD rats showed no pathological damage or adverse effects on these organs at either 30 or 60 d after implantation (Fig. 13b).

To further validate the degradation and histocompatibility of the alloys, a subcutaneous implantation animal model was further employed. The *in vivo* degradation of Mg alloys was observed to be relatively rapid, leading to the accumulation of H_2, which could affect the surrounding tissues and effectiveness of the implants. The situation during tissue sampling is shown in Fig. S8, where no obvious gas accumulation was observed in any of the groups during the early stages, likely because of inadequate tissue encapsulation. As tissue encapsulation gradually occurred around the materials, the gas was confined to the vicinity of the materials. At 15 d, the FSP-800 material exhibited the least gas accumulation compared with the other groups. At 30 d, gas accumulation significantly decreased around the FSP-300 and FSP-800 materials, whereas it progressively increased in the BM group. At 60 d, owing to a decrease in the degradation rate, no gas cavities were formed around the FSP-300 and FSP-800 materials, whereas the BM material remained enveloped by gas. Therefore, the FSP-800 sample demonstrated the highest biocompatibility, exhibiting negligible negative effects on the organism. Observations of the subcutaneous tissues surrounding the implanted samples (Fig. 13a) revealed that all implants underwent degradation, producing H_2 that accumulated in the subcutaneous tissue and formed bubbles. Histological analysis of the surrounding tissues of the implanted materials in each group, as shown in Fig. 13a, demonstrated that local tissue inflammation was induced in all

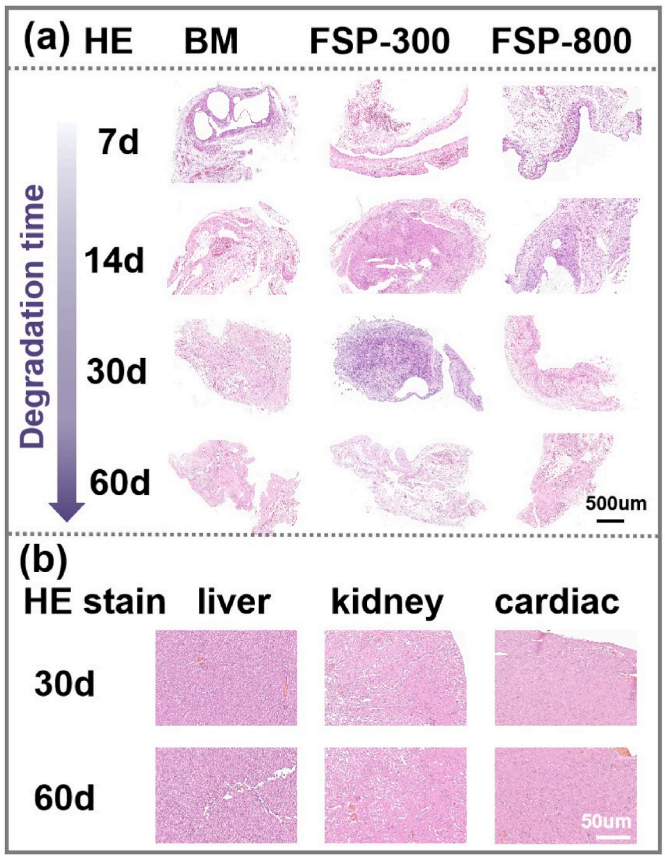

Fig. 13. (a) Photomicrographs of subcutaneous tissue sections of BM, FSP-300, and FSP-800 after subcutaneous implantation for 7, 14, 30, and 60 d. (b) H&E staining of the liver, kidney, and cardiac organs after implantation of alloys for 30 and 60 d.

samples in the early stages of implantation but gradually subsided over time. Importantly, the FSP-800 samples exhibited milder inflammatory reactions and a thinner fibrous layer than the other groups, indicating the superior *in vivo* histocompatibility of FSP-800 implants.

M1 macrophages (CD86) play a significant role in inflammatory responses, whereas M2 macrophages (CD206) are crucial for tissue repair. Therefore, immunohistochemical staining of the soft tissue surrounding the alloy can facilitate the evaluation of the degree of inflammatory response, thereby assessing biosafety (Fig. 14). Immunohistochemical staining quantification results were adopted to detect the effects of inflammatory tissue on the expression of the angiogenesis-related markers CD86 and CD206 in the tissue surrounding the alloys. The results indicated that at the 7- and 14-day time points, the number of cells expressing CD86 in the tissues surrounding the BM was significantly higher than that in FSP-300 and FSP-800. However, at the 30- and 60-day time points, there was no significant difference in the expression of CD86 in the tissues surrounding the alloy between the groups. At the 7- and 14-day time points, there was no obvious difference in the expression of CD206 in the tissues surrounding the alloy. However, the expression of CD206 in FSP-800 was significantly higher than that in the other samples at the 30- and 60-day time points.

4. Discussion

4.1. Roles of FSP in the formation of surface film during the biodegradation of WEJ431 alloys

It is well established that factors such as grain size, precipitated phases, and dislocation density directly affect the corrosion of Mg alloys

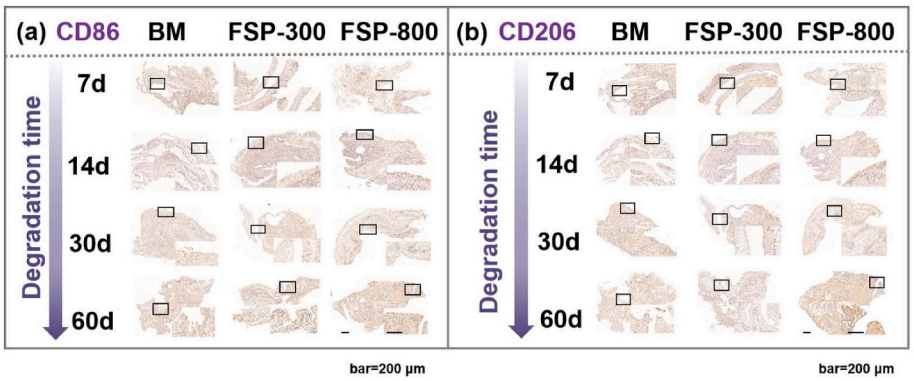

Fig. 14. Macromorphological and immunohistochemical (CD86 and CD206) observations of BM, FSP-300, and FSP-800 implants located in subcutaneous tissue at different time points.

[22,57]. In this study, subjecting the WEJ431 alloy to FSP resulted in grain refinement, which promoted the formation of a denser surface film to enhance corrosion resistance. Nevertheless, the degradation behavior of the cast WEJ431 Mg alloy system with numerous dendritic precipitated phases may be affected more by the differences in the precipitates. The volume, size, and distribution of the precipitated phases significantly influence the evolution of the surface film during corrosion process [58–60]. Cross-sectional SEM images of corroded samples were investigated. As shown in Fig. 15a and b, a thick and nonuniform corrosion product film was generated on the BM surface with diverse local detachments and cracks. The corrosion cross-section of the BM was uneven with many large corrosion pits on the surface, leading to the collapse of the BM sample in the later stage of the corrosion process. After the FSP, a denser corrosion product film was deposited on the surface (Fig. 15c–f). Although there were some slight corrosion pits at the interface between the product film and the substrate after immersion for 30 d, a uniform degradation process was achieved on the FSP-treated alloys. Notably, the surface of the corroded FSP-800 sample was quite flat with almost no corrosion depression at the interface, indicating a uniform and slow degradation process. Simultaneously, a dense film

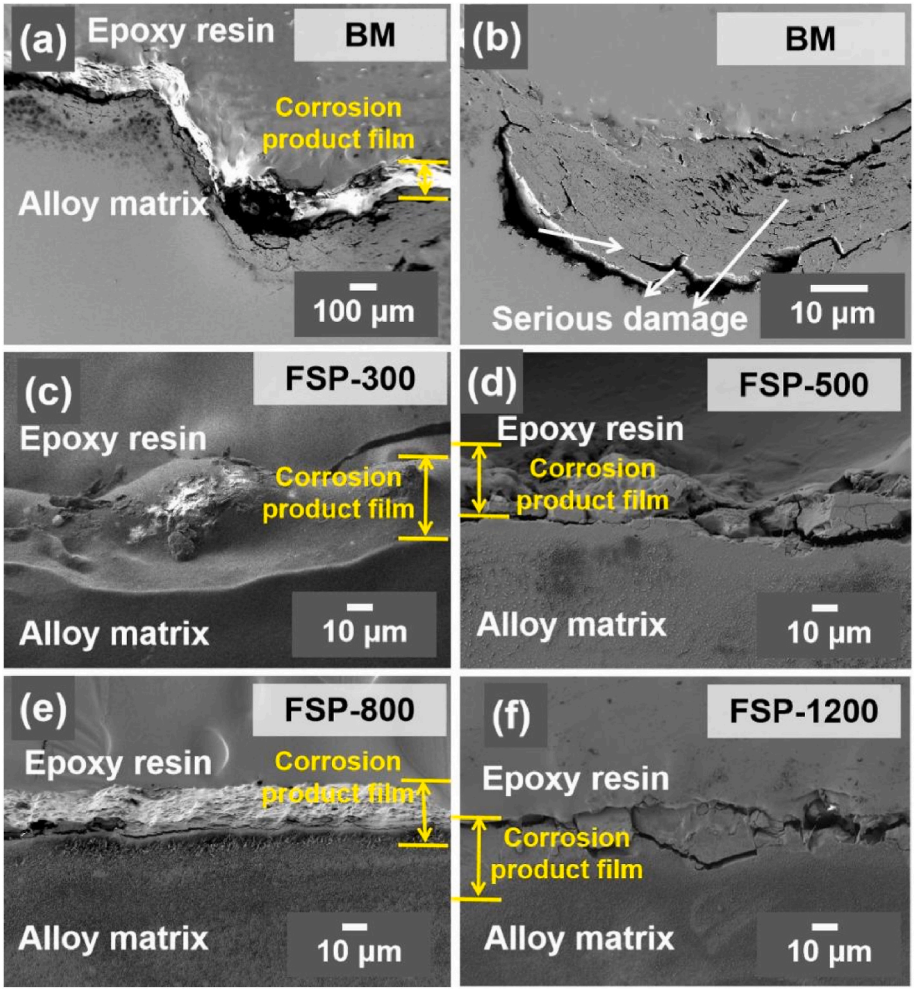

Fig. 15. SEM images of cross-sections of (a, b) BM, (c) FSP-300, (d) FSP-500, (e) FSP-800, and (f) FSP-1200 after immersion in Hanks' solution for 30 d.

with a thickness of 14 μm was generated on the surface of the FSP-800 sample (Fig. 15e). To gain a deeper understanding of the corrosion behavior, the XRD patterns of these alloys after immersion for 30 d were obtained to identify the chemistry of the surface film. As shown in Fig. 16a, the characteristic peaks of $Mg(OH)_2$ were detected using XRD. Meanwhile, a large amount of calcium phosphate was deposited on these alloys during degradation. New peaks of $Y(OH)_3$ appeared in the XRD patterns of the FSP-treated alloys after degradation, indicating that the deposition rate of $Y(OH)_3$ in the FSP-treated WEJ431 alloy was much faster than that in the BM (Fig. 16b). Y_2O_3 and $Nd(OH)_3$ were also detected in the XRD patterns. In fact, oxides or hydroxides containing rare earth elements have stronger passivity and protection than magnesium hydroxide, which can effectively prevent severe attacks on the alloy matrix [61]. The FSP-800 sample exhibited the strongest characteristic peaks of $Y(OH)_3/Y_2O_3$ and $Nd(OH)_3$, which promoted the formation of a protective layer that resisted corrosion.

4.2. Roles of FSP in the galvanic corrosion of WEJ431 alloys

In Mg-RE alloys, the second phase acts as a cathodic site for the α-Mg phase, resulting in anodic dissolution and the loss of precipitates [54]. Generally, the volume, size, and distribution of the precipitated phases significantly affect the galvanic corrosion of an alloy [62]. The surface roughness of these alloys after corrosion was investigated using laser microscopy, and the corrosion products generated on the surfaces were cleaned. As depicted in Fig. 17a, localized corrosion attacks and pits extend in depth, leading to severe non-uniform corrosion of the BM. The profile results suggested that the maximum corrosion depth was nearly 784.4 μm after immersion in Hanks' solution for 30 d (Fig. 17f). Fig. 17b, c, e, and f show that the corrosion depths of FSP-300, FSP-500, and FSP-1200 decreased to approximately 199.5 μm, 107.8 μm, and 61.4 μm, respectively. FSP-800 exhibited a very uniform and flat surface after the long-term corrosion process (Fig. 17d), with the corrosion depth decreasing to 12.9 μm. This clearly illustrates that the FSP-800 sample exhibited the best corrosion resistance and achieved a uniform degradation process. In the FSP process, the precipitates were refined and distributed uniformly, and some alloying RE elements were dissolved back into the Mg matrix as an α-Mg solid solution. This unique microstructure of the FSP-treated alloy endowed it with the ability to resist micro-galvanic corrosion between the precipitates and Mg matrix.

4.3. Biosafety and biocompatibility in vitro and in vivo

In this study, the researchers also placed emphasis on evaluating the *in vivo* biosafety and biocompatibility of the biomaterials. Degradation of Mg alloys can result in the generation of hydrogen gas (H_2), hydroxide ions (OH^-), free magnesium ions (Mg^{2+}), rare earth (RE), and strontium (Sr) ions. These byproducts have the potential to cause damage to surrounding tissues or the body as a whole. To investigate whether the samples induced liver toxicity, the plasma levels of ASAT and ALAT were measured. An increase in the levels of these enzymes can be considered as a key indicator of hepatocellular injury.

The ALAT and ASAT levels returned to normal in all groups after 14 d, as compared to those in the control group (Figs. S9a–c). The ASAT and creatinine levels of BM were significantly higher than those of the FSP-300 and FSP-800 alloys after 24 h, suggesting that, at least within the first 24 h, the biosafety of BM was not satisfactory and affected the function of the liver and kidney. Although these levels returned to the lower level at 7 d, indicating no long-term liver dysfunction and kidney function damage, there was no significant damage to liver and kidney function at any time point in FSP-300 and FSP-800. This indicates that these alloys had better biological safety than the control group. Based on the characteristics of the degradation curves of the materials *in vivo* and *in vitro*, their biological safety was positively correlated with the material degradation rate. This indicates that materials with slower degradation rates may exhibit better biological safety profiles.

The potential inflammatory effect of the biomaterial was evaluated by monitoring plasma levels of IL-6. The IL-6 values remained below the toxicity threshold and aligned with normal function, as reported in the literature (30 μmol/L) [63]. Compared with the control group, IL-6 levels exhibited no significant changes at 24 h, 7 d, and 14 d (Fig. S9d).

These findings, along with histological analysis, indicate that even with the accumulation of Mg, RE, and Sr in the liver, there was no discernible impact on hepatic function. The results confirmed that FSP-800 implantation was the safest option compared to the control group, as it did not induce acute or chronic toxicity or cause weight loss in the animals (Fig. S8). Additionally, the temporary increase in IL-6 levels can be attributed to surgery and then returned to normal values after 7 d, suggesting the absence of prolonged inflammation. Taken together, these results provide evidence that the accumulation of small amounts of metal ions (Mg, RE, and Sr) in the liver and kidney during alloy degradation did not affect organ function.

Macrophage polarization plays a crucial role in tissue inflammation. Polarization states from M1 to M2 have been verified through *in vitro* studies by investigating morphological phenotype markers (CD86 or CD206), which can help assess the degree of tissue inflammation and indirectly reflect the biosafety of the encapsulated biomaterials. Because of the rapid early degradation of the alloy in the body, chemical stimulation of the surrounding tissues by the alkaline products produced and physical stimulation of the surrounding tissues by the accumulation of hydrogen are important reasons for the inflammatory state (high CD86 expression) of the tissues surrounding the alloy. Therefore, the expression of local inflammatory responses in various materials is positively correlated with their degradation rates. FSP-800, which degraded the

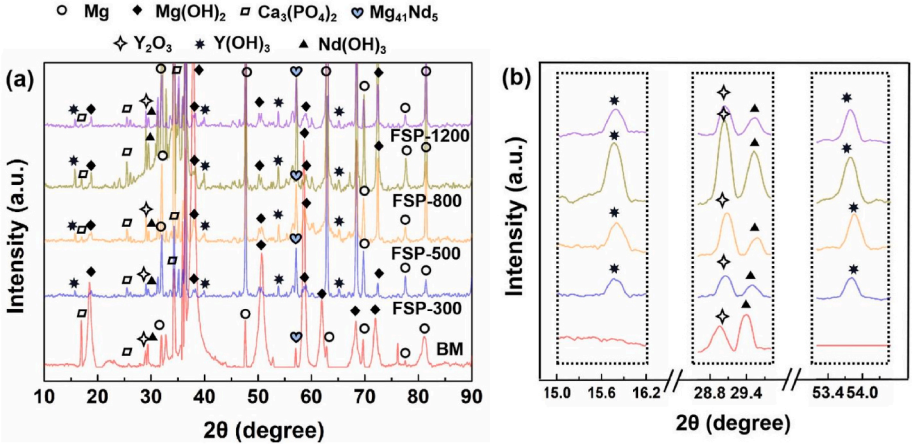

Fig. 16. XRD patterns of BM, FSP-300, FSP-500, FSP-800, and FSP-1200 after immersion in Hanks' solution for 30 d.

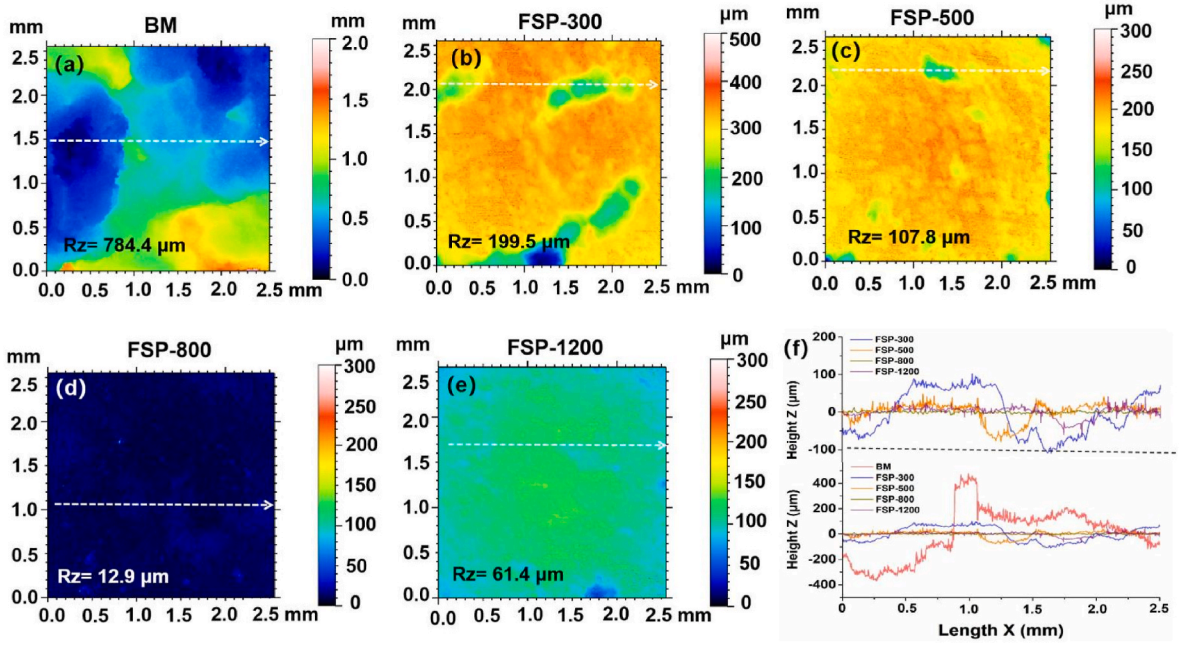

Fig. 17. Laser microscopy images of (a) BM, (b) FSP-300, (c) FSP-500, (d) FSP-800, and (e) FSP-1200 after 30 d of immersion in Hanks' solution. (f) Corrosion depth profiles of the lines in (a)–(e).

slowest *in vitro* and *in vivo*, showed the best biosafety in the early stages of implantation (7 and 14 d), with minimal inflammatory response in the surrounding tissues. At 60 d, because the degradation rate of the Mg alloys in all groups dropped to similar levels, there was no significant difference in the inflammatory response among the groups. Macrophages that express CD206 are generally thought to promote tissue repair. Immunohistochemistry showed no significant changes in each group at the 7-, 14-, and 30-day time points; however, only at 60 d in the FSP-800 group did the tissue show higher expression of CD206 than the other groups. Although it was difficult to conclude that the FSP-800 alloy played a definite role in inducing tissue repair, the early low-level inflammatory response in the surrounding tissues was crucial for tissue repair and better biosafety. This suggests that the FSP-800 alloy is a promising material for biomedical applications owing to its superior biosafety profile.

4.4. Degradation mechanism

Traditional commercial Mg alloys, particularly Mg-RE alloys, exhibit severe micro-galvanic corrosion because of the presence of numerous cathodic phases, which are known to be more passive than the anodic Mg matrix [64,65]. The dissolution of the anodic α-Mg phases gradually

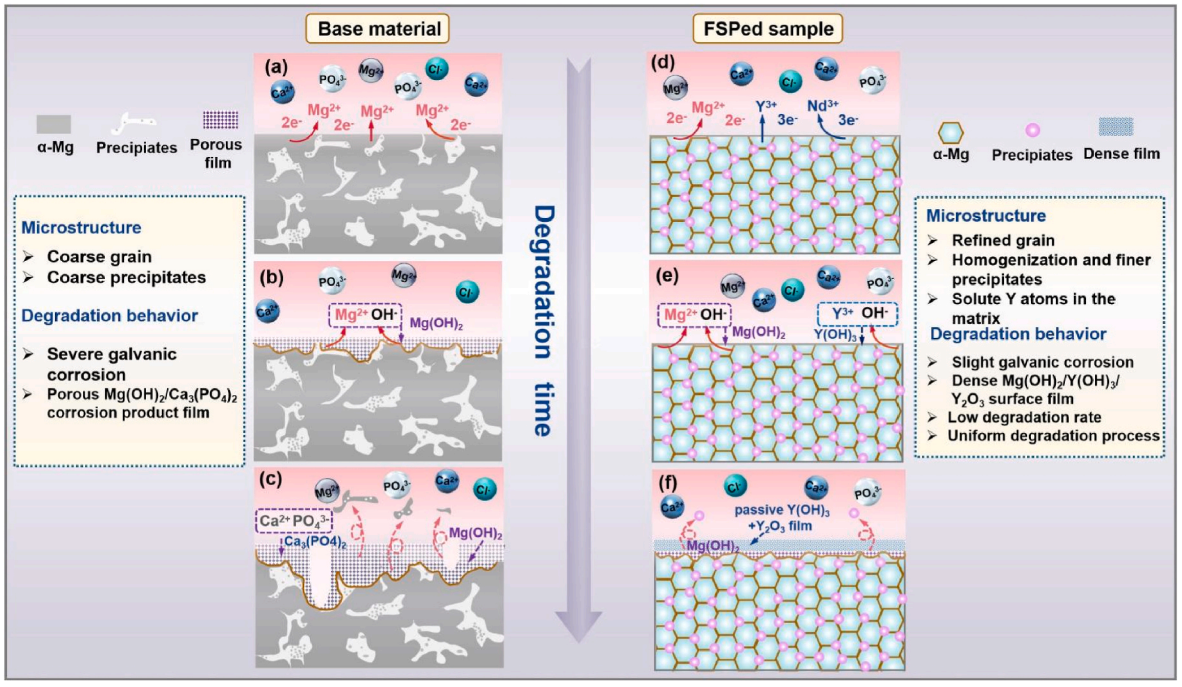

Fig. 18. Illustration of degradation mechanism of (a–c) BM- and (d–f) FSP-treated samples.

forms a $Mg(OH)_2$/MgO surface film during the immersion period. However, the loose and porous $Mg(OH)_2$ film struggles to provide sufficient protection to the metallic substrate, which can exacerbate galvanic corrosion [66]. Microstructural evolution, including grain size, crystal orientation, and changes in precipitated phases, plays a significant role in corrosion behavior [9,24,67]. Based on the above *in vitro* and *in vivo* degradation analyses, the degradation mechanism in this study was generalized and summarized as follows (Fig. 18). In the BM, coarse Mg-RE-precipitated phases in the Mg matrix significantly contributed to the severe galvanic corrosion. In the initial stage of degradation, the Mg-RE precipitates were less active than the α-Mg phases, and degradation began with the α-Mg matrix (Fig. 18a). As illustrated in Fig. 18b, with the continuous dissolution of the α-Mg matrix, the corrosion gradually extended along the boundary of the precipitated Mg-RE phases. The extension of the micro-galvanic corrosion resulted in a large shedding area for the matrix, and further corrosion caused the precipitated phases to peel off. Subsequently, the loose $Mg(OH)_2$ surface film barely provided a barrier effect, leading to large corrosion pits on the BM surface during the last stage of degradation (Fig. 18c). Similarly, the *in vivo* degradation of BM was relatively fast, and the resulting hydrogen accumulation affected the surrounding tissue or influenced the effect of the implant through precipitation at the implant-tissue interface when used as orthopedic implants.

FSP modified the microstructure of the alloy, resulting in refined grains, finer and homogenized precipitates, and a Mg matrix with a high dissolution of RE elements. In fact, research has confirmed that when the precipitated phases become very fine (below the critical size or near the nanometer level), their dispersed distribution can mitigate galvanic corrosion [35,68]. Finer and re-distributed precipitates can create a more "electrochemically homogenous" microstructure [36]. Simultaneously, the high content of solute RE elements in the Mg matrix played a key role in forming a dense surface film. When exposed to *in vivo* conditions, the solutes Y that initially dissolved in the Mg matrix formed $Y(OH)_3/Y_2O_3$ deposited on the surface, providing strong protection for the underlying metallic substrate (Fig. 18d–f). However, the Y and Nd atoms in the precipitates hardly dissolved because they served as cathode phases protected by the Mg matrix. Therefore, it was difficult to form a dense surface film with a high RE content in BM. For the FSP-treated alloys, slight galvanic corrosion and dense surface film jointly endowed the samples with a low degradation rate and uniform degradation. Its specific performance is as follows. On the one hand, little H_2 accumulated in the FSP-treated alloys during degradation. *In vivo* degradation showed no obvious H_2 cavity formation around the FSP-800 and FSP-300 samples at the 30 and 60 d observation time points; only a few bubbles were observed at 15 d. Song [9] reported that the daily hydrogen release rate of 0.01 mL cm^2 can be tolerated by the human body without causing damage. Therefore, we inferred that the H_2 evolution rate of the FSP-treated samples *in vivo* was lower than 0.01 mL/cm^2 per day. Witte et al. [69] demonstrated that the corrosion rate at subcutaneous implantation was significantly higher than that in the bone. Therefore, we speculated that the amount of H_2 evolution in FSP-800 and FSP-300 alloys in the bone would be further reduced. On the other hand, the FSP-800 implant incredibly achieved a superior *in vivo* corrosion rate of approximately 0.09 mm/y, which was much lower than almost all of the candidate Mg implant materials reported before [12,28,37,43,70,71].

The samples underwent varying degrees of *in vitro* and *in vivo* degradation over time, with the corrosion rate *in vivo* being lower than that *in vitro*. Compared with *in vitro* degradation (immersion in Hank's solution), Mg alloys or other implant materials faced a very complex environment during the *in vivo* degradation process. *In vitro*, Mg alloys dissolved in corrosive media and gradually released large amounts of H_2. Because there was no dense packaging in this environment, the corrosion process of the exposed Mg alloys was continuously aggravated. This also explained why the hydrogen evolution rate of BM increased rapidly in the later stages of corrosion (Fig. 8a). For the FSP-treated samples, the alloys formed a dense protective film to decelerate material degradation, although this feature was weakened. Factors such as body fluid immersion, inflammatory response, tissue wrapping, and air cavity formation all affected the degradation of Mg alloys *in vivo*. The implant in the body was wrapped with biological tissue; thus, the alloys were not completely exposed to the environment. Compared with *in vitro* degradation, *in vivo* degradation can initiate uniform degradation more easily after the formation of a stable surface film on the implant surface (Fig. S10). Therefore, the degradation rate of the implanted materials *in vivo* was lower than that *in vitro*. FSP-treated implants, with their denser surface films and lower immune and inflammatory responses, showed greater advantages during *in vivo* degradation. Consequently, the *in vivo* degradation rate was very low.

4.5. Future developments and research directions

This study demonstrated significant improvements in the *in vitro* and *in vivo* degradation properties of biodegradable Mg alloys using the FSP technique. These advancements in biocompatibility and degradation characteristics indicate great potential for the clinical application of FSPed alloys. Nevertheless, several unresolved issues remain that warrant attention in future research. This study preliminarily demonstrated the potential of the FSP technique to enhance the *in vivo* degradation performance of Mg alloys. However, the actual orthopaedic clinic environment is complex. Further *in vivo* implant tests, such as intramedullary nail studies, are necessary to validate degradation performance. Additionally, long-term biotoxicity monitoring is essential to establish the biosafety of these materials. Moreover, although FSP can process large-scale implants in the biomedical field through a horizontal multi-pass process, intensive research is required to characterize the interfaces between these layers. These issues will require careful investigation in future studies.

5. Conclusions

In this study, a WEJ431 alloy was designed and subjected to friction stir processing (FSP) to obtain an ideal biodegradable Mg alloy for implant applications. The microstructure, mechanical properties, *in vitro* and *in vivo* degradation processes, and biocompatibility of the alloys were thoroughly investigated. The main findings of this study can be summarized as follows:

(1) The application of FSP to the WEJ431 alloy resulted in a modification of the microstructure, leading to refined grains, high-solute RE elements in the matrix, and a uniform distribution of finer precipitates. The grain size of the alloy was effectively refined from 53.5 μm to 3.4 μm after FSP with a rotation speed of 800 rpm. Additionally, the FSP-800 sample exhibited a higher solid solution content of Y/Nd.

(2) The mechanical strength and elongation of the alloys were significantly enhanced after the FSP. The tensile strength of the alloys increased with increasing tool rotation speed. When the rotation speed was increased to 1200 rpm, the YS and UTS improved to 190.5 MPa and 267.6 MPa, respectively. The EI reached its maximum value (8 %) at a rotation speed of 800 rpm. The grain refinement, precipitate strengthening, and dislocation strengthening collectively increased the strength and elongation of the FSP-treated alloy.

(3) *In vitro* experiments demonstrated that after FSP, the alloy exhibited an extremely low corrosion current density, hydrogen evolution volume, and corrosion rate. Specifically, the *in vitro* corrosion rate of the alloys after FSP significantly decreased by 82.9 %–93.9 % compared to that of the BM. The FSP-800 variant exhibited the best *in vitro* corrosion resistance and the most uniform degradation behavior, with the corrosion depth decreasing to 12.9 μm.

(4) *In vivo* degradation tests were performed on the BM, FSP-300, and FSP-800 by implanting these samples into rats (12 weeks old). The 3D micro-CT results showed that FSP led to superior uniform *in vivo* degradation behavior for the WEJ431 alloys. More importantly, the FSP-800 implants exhibited an extremely low *in vivo* degradation rate of 0.09 mm/y, which was lower than most of the candidate Mg implant materials reported before. These samples exhibited excellent biocompatibility and did not cause undesirable inflammation or produce toxic corrosion products.

(5) The homogeneous distribution of finer precipitates in the WEJ431 alloy after FSP effectively hindered the micro-galvanic corrosion. Additionally, the solutes of the Y atoms in the matrix contributed to the formation of a dense and passive $Y(OH)_3/Y_2O_3$ surface film. The synergistic effect of the slight galvanic corrosion and dense surface film resulted in a superior degradation behavior.

Ethics approval and consent to participate

The Animal Care and Experiment Committee and Animal Ethics Committee of the First Affiliated Hospital of Chongqing Medical University (No. 20187801) approved all the animal experiments conducted in this study.

CRediT authorship contribution statement

Yixing Zhu: Writing – review & editing, Writing – original draft, Validation, Methodology, Investigation, Formal analysis. **Mengran Zhou:** Writing – review & editing, Validation, Supervision, Resources, Conceptualization. **Weikang Zhao:** Writing – review & editing, Writing – original draft, Validation, Resources, Methodology, Investigation. **Yingxin Geng:** Writing – review & editing, Investigation. **Yujie Chen:** Writing – review & editing, Methodology, Investigation. **Han Tian:** Writing – review & editing, Methodology, Investigation. **Yifan Zhou:** Writing – review & editing, Investigation. **Gaoqiang Chen:** Writing – review & editing, Supervision, Resources. **Ruizhi Wu:** Writing – review & editing, Methodology. **Yufeng Zheng:** Writing – review & editing, Conceptualization. **Qingyu Shi:** Writing – review & editing, Supervision, Resources, Methodology, Conceptualization.

Declaration of competing interest

Yufeng Zheng is an editor-in-chief for Bioactive Materials and was not involved in the editorial review or the decision to publish this article. All authors declare that there are no competing interests.

Acknowledgements

This study was financially supported by the National Natural Science Foundation of China (Grant No. 52305385, Grant No. U23A20541 and Grant No. 82102571), the China Postdoctoral Science Foundation (2022M710564) and Chongqing Natural Science Foundation (CSTB2022NSCQ-MSX0089).

Appendix A. Supplementary data

Supplementary data to this article can be found online at https://doi.org/10.1016/j.bioactmat.2024.07.021.

References

[1] N. Singh, U. Batra, K. Kumar, N. Ahuja, A. Mahapatro, Progress in bioactive surface coatings on biodegradable Mg alloys: a critical review towards clinical translation, Bioact. Mater. 19 (2023) 717–757.
[2] M.S. Dargusch, N. Balasubramani, N. Yang, S. Johnston, Y. Ali, G. Wang, J. Venezuela, J. Carluccio, C. Lau, R. Allavena, D. Liang, K. Mardon, Q. Ye, In vivo performance of a rare earth free Mg-Zn-Ca alloy manufactured using twin roll casting for potential applications in the cranial and maxillofacial fixation devices, Bioact. Mater. 12 (2022) 85–96.
[3] F. Xing, S. Li, D. Yin, J. Xie, P.M. Rommens, Z. Xiang, M. Liu, U. Ritz, Recent progress in Mg-based alloys as a novel bioabsorbable biomaterials for orthopedic applications, J. Magnesium Alloys 10 (2022) 1428–1456.
[4] M.P. Staiger, A.M. Pietak, J. Huadmai, G. Dias, Magnesium and its alloys as orthopedic biomaterials: a review, Biomaterials 27 (2006) 1728–1734.
[5] H.Q. Ang, T.B. Abbott, S. Zhu, C. Gu, M.A. Easton, Proof stress measurement of die-cast magnesium alloys, Mater. Des. 112 (2016) 402–409.
[6] H. Shi, C. Xu, X. Hu, W. Gan, K. Wu, X. Wang, Improving the Young's modulus of Mg via alloying and compositing – a short review, J. Magnesium Alloys 10 (2022) 2009–2024.
[7] Y. Yang, C. He, E. Dianyu, W. Yang, F. Qi, D. Xie, L. Shen, S. Peng, C. Shuai, Mg bone implant: features, developments and perspectives, Mater. Des. 185 (2020) 108259.
[8] Y. Ogawa, D. Ando, Y. Sutou, J. Koike, A lightweight shape-memory magnesium alloy, Science 353 (2016) 368–370.
[9] G. Song, Control of biodegradation of biocompatable magnesium alloys, Corrosion Sci. 49 (2007) 1696–1701.
[10] D. Bairagi, S. Mandal, A comprehensive review on biocompatible Mg-based alloys as temporary orthopaedic implants: current status, challenges, and future prospects, J. Magnesium Alloys 10 (2022) 627–669.
[11] A. Atrens, S. Johnston, Z. Shi, M.S. Dargusch, Viewpoint - understanding Mg corrosion in the body for biodegradable medical implants, Scripta Mater. 154 (2018) 92–100.
[12] Y. Chen, Z. Xu, C. Smith, J. Sankar, Recent advances on the development of magnesium alloys for biodegradable implants, Acta Biomater. 10 (2014) 4561–4573.
[13] Z. Zeng, M. Zhou, P. Lynch, F. Mompiou, Q. Gu, M. Esmaily, Y. Yan, Y. Qiu, S. Xu, H. Fujii, C. Davies, J.-F. Nie, N. Birbilis, Deformation modes during room temperature tension of fine-grained pure magnesium, Acta Mater. 206 (2021) 116648.
[14] Z. Li, X. Gu, S. Lou, Y. Zheng, The development of binary Mg-Ca alloys for use as biodegradable materials within bone, Biomaterials 29 (2008) 1329–1344.
[15] L.-X. Long, F.-F. Chen, L.-Y. Cui, Z.-S. Wei, H.-T. Wang, R.-C. Zeng, Y.-F. Zheng, Comparison of microstructure, mechanical property, and degradation rate of Mg–1Li–1Ca and Mg–4Li–1Ca alloys, Bioact. Mater. 26 (2023) 279–291.
[16] H. Pan, K. Pang, F. Cui, F. Ge, C. Man, X. Wang, Z. Cui, Effect of alloyed Sr on the microstructure and corrosion behavior of biodegradable Mg-Zn-Mn alloy in Hanks' solution, Corrosion Sci. 157 (2019) 420–437.
[17] F. Rosalbino, S. De Negri, A. Saccone, E. Angelini, S. Delfino, Bio-corrosion characterization of Mg-Zn-X (X = Ca, Mn, Si) alloys for biomedical applications, Journal of materials science, Mater. Med. 21 (2010) 1091–1098.
[18] K. Munir, J. Lin, C. Wen, P.F.A. Wright, Y. Li, Mechanical, corrosion, and biocompatibility properties of Mg-Zr-Sr-Sc alloys for biodegradable implant applications, Acta Biomater. 102 (2020) 493–507.
[19] A. Torroni, C. Xiang, L. Witek, E.D. Rodriguez, P.G. Coelho, N. Gupta, Biocompatibility and degradation properties of WE43 Mg alloys with and without heat treatment: in vivo evaluation and comparison in a cranial bone sheep model, J. Cranio-Maxillo-Facial Surg. : Off. Publ. Eur. Assoc. Cranio-Maxillo-Facial Surg. 45 (2017) 2075–2083.
[20] D. Liu, D. Yang, X. Li, S. Hu, Mechanical properties, corrosion resistance and biocompatibilities of degradable Mg-RE alloys: a review, J. Mater. Res. Technol. 8 (2019) 1538–1549.
[21] J. Bennett, Q. De Hemptinne, K. McCutcheon, Magmaris resorbable magnesium scaffold for the treatment of coronary heart disease: overview of its safety and efficacy, Expet Rev. Med. Dev. 16 (2019) 757–769.
[22] A.D. Sudholz, K. Gusieva, X.B. Chen, B.C. Muddle, M.A. Gibson, N. Birbilis, Electrochemical behaviour and corrosion of Mg–Y alloys, Corrosion Sci. 53 (2011) 2277–2282.
[23] N. Birbilis, M.A. Easton, A.D. Sudholz, S.M. Zhu, M.A. Gibson, On the corrosion of binary magnesium-rare earth alloys, Corrosion Sci. 51 (2009) 683–689.
[24] B. Feng, G. Liu, P. Yang, S. Huang, D. Qi, P. Chen, C. Wang, J. Du, S. Zhang, J. Liu, Different role of second phase in the micro-galvanic corrosion of WE43 Mg alloy in NaCl and Na2SO4 solution, J. Magnesium Alloys 10 (2022) 1598–1608.
[25] H. Hermawan, D. Dube, D. Mantovani, Developments in metallic biodegradable stents, Acta Biomater. 6 (2010) 1693–1697.
[26] Y.F. Zheng, X.N. Gu, F. Witte, Biodegradable metals, Mater. Sci. Eng. R Rep. 77 (2014) 1–34.
[27] Y. Shen, J. Chen, G. Wang, D. Cao, L. Tan, R.D.K. Misra, K. Yang, Effects of ECAP extrusion on the mechanical and biodegradable properties of an extruded Mg-1.5Zn-0.5Y-0.5Zr alloy, Mater. Technol. 37 (2020) 135–142.
[28] S. Zhang, X. Zhang, C. Zhao, J. Li, Y. Song, C. Xie, H. Tao, Y. Zhang, Y. He, Y. Jiang, Y. Bian, Research on an Mg-Zn alloy as a degradable biomaterial, Acta Biomater. 6 (2010) 626–640.
[29] W. Wang, C. Blawert, R. Zan, Y. Sun, H. Peng, J. Ni, P. Han, T. Suo, Y. Song, S. Zhang, M.L. Zheludkevich, X. Zhang, A novel lean alloy of biodegradable Mg–2Zn with nanograins, Bioact. Mater. 6 (2021) 4333–4341.
[30] E.V. Parfenov, O.B. Kulyasova, V.R. Mukaeva, B. Mingo, R.G. Farrakhov, Y. V. Cherneikina, A. Yerokhin, Y.F. Zheng, R.Z. Valiev, Influence of ultra-fine grain structure on corrosion behaviour of biodegradable Mg-1Ca alloy, Corrosion Sci. 163 (2020) 108303.
[31] A.R. Eivani, M. Mehdizade, S. Chabok, J. Zhou, Applying multi-pass friction stir processing to refine the microstructure and enhance the strength, ductility and corrosion resistance of WE43 magnesium alloy, J. Mater. Res. Technol. 12 (2021) 1946–1957.

[32] R.S. Mishra, Z.Y. Ma, Friction stir welding and processing, Mater. Sci. Eng. R Rep. 50 (2005) 1–78.
[33] W. Wang, X. Meng, W. Dong, Y. Xie, X. Ma, D. Mao, Z. Zhang, Y. Huang, In-situ rolling friction stir welding of aluminum alloys towards corrosion resistance, Corrosion Sci. 230 (2024) 111920.
[34] B. Mansoor, A.K. Ghosh, Microstructure and tensile behavior of a friction stir processed magnesium alloy, Acta Mater. 60 (2012) 5079–5088.
[35] Y. Zhu, G. Chen, Y. Zhou, Q. Shi, M. Zhou, Achieving synergistic strength-ductility-corrosion optimization in Mg-Li-Al-Zn alloy via cross-pass friction stir processing, J. Alloys Compd. 959 (2023) 170581.
[36] Q. Liu, Q.-x. Ma, G.-q. Chen, X. Cao, S. Zhang, J.-l. Pan, G. Zhang, Q.-y. Shi, Enhanced corrosion resistance of AZ91 magnesium alloy through refinement and homogenization of surface microstructure by friction stir processing, Corrosion Sci. 138 (2018) 284–296.
[37] V.C. Shunmugasamy, M. AbdelGawad, M.U. Sohail, T. Ibrahim, T. Khan, T.D. Seers, B. Mansoor, In vitro and in vivo study on fine-grained Mg–Zn–RE–Zr alloy as a biodegradeable orthopedic implant produced by friction stir processing, Bioact. Mater. 28 (2023) 448–466.
[38] K. Nakata, Y.G. Kim, H. Fujii, T. Tsumura, T. Komazaki, Improvement of mechanical properties of aluminum die casting alloy by multi-pass friction stir processing, Mater. Sci. Eng., A 437 (2006) 274–280.
[39] X. Meng, Y. Huang, J. Cao, J. Shen, J.F. dos Santos, Recent progress on control strategies for inherent issues in friction stir welding, Prog. Mater. Sci. 115 (2021) 100706.
[40] B. Bagheri, M. Abbasi, Development of AZ91/SiC surface composite by FSP: effect of vibration and process parameters on microstructure and mechanical characteristics, Adv. Manuf. 8 (2020) 82–96.
[41] M. Cheng, J. Chen, H. Yan, B. Su, Z. Yu, W. Xia, X. Gong, Effects of minor Sr addition on microstructure, mechanical and bio-corrosion properties of the Mg-5Zn based alloy system, J. Alloys Compd. 691 (2017) 95–102.
[42] J.-H. Dong, L.-L. Tan, Y.-B. Ren, K. Yang, Effect of microstructure on corrosion behavior of Mg–Sr alloy in hank's solution, Acta Metall. Sin. 32 (2018) 305–320.
[43] X.N. Gu, X.H. Xie, N. Li, Y.F. Zheng, L. Qin, In vitro and in vivo studies on a Mg–Sr binary alloy system developed as a new kind of biodegradable metal, Acta Biomater. 8 (2012) 2360–2374.
[44] F. Cao, C. Zhao, G.-L. Song, D. Zheng, The corrosion of pure Mg accelerated by haze pollutant ammonium sulphate, Corrosion Sci. 150 (2019) 161–174.
[45] W. Zhao, J. Wang, J. Weiyang, B. Qiao, Y. Wang, Y. Li, D. Jiang, A novel biodegradable Mg-1Zn-0.5Sn alloy: mechanical properties, corrosion behavior, biocompatibility, and antibacterial activity, J. Magnesium Alloys 8 (2020) 374–386.
[46] C. Zhang, C. Liu, X. Li, K. Liu, G. Tian, J. Wang, Quantifying the influence of secondary phases on corrosion in multicomponent Mg alloys using X-ray computed microtomography, Corrosion Sci. 195 (2022) 110010.
[47] W.T. Sun, C. Xu, X.G. Qiao, M.Y. Zheng, S. Kamado, N. Gao, M.J. Starink, Evolution of microstructure and mechanical properties of an as-cast Mg-8.2Gd-3.8Y-1.0Zn-0.4Zr alloy processed by high pressure torsion, Mater. Sci. Eng., A 700 (2017) 312–320.
[48] L. Gao, R.S. Chen, E.H. Han, Effects of rare-earth elements Gd and Y on the solid solution strengthening of Mg alloys, J. Alloys Compd. 481 (2009) 379–384.
[49] D. Buey, L.G. Hector, M. Ghazisaeidi, Core structure and solute strengthening of second-order pyramidal ⟨c+a⟩ dislocations in Mg-Y alloys, Acta Mater. 147 (2018) 1–9.
[50] J. Peng, Z. Zhang, Z. Liu, Y. Li, P. Guo, W. Zhou, Y. Wu, The effect of texture and grain size on improving the mechanical properties of Mg-Al-Zn alloys by friction stir processing, Sci. Rep. 8 (2018).
[51] J.-F. Nie, Precipitation and hardening in magnesium alloys, Metall. Mater. Trans. 43 (2012) 3891–3939.
[52] Z. Jiang, J. Zhang, D. Shi, C. Lei, Quasi-in-situ EBSD study on the influence of precipitations on the strength, plasticity and deformation mechanism in Al–Cu–Li alloys, Met. Mater. Int. 30 (2024) 1895–1909.
[53] Y.-X. Zhu, G.-L. Song, P.-P. Wu, D.-J. Zheng, Z.-M. Wang, A burnished and Al-alloyed magnesium surface with improved mechanical and corrosion properties, Corrosion Sci. 184 (2021) 109395.
[54] M. AbdelGawad, C.A. Usman, V.C. Shunmugasamy, I. Karaman, B. Mansoor, Corrosion behavior of Mg-Zn-Zr-RE alloys under physiological environment – impact on mechanical integrity and biocompatibility, J. Magnesium Alloys 10 (2022) 1542–1572.
[55] J. Huang, G.-L. Song, Y. Zhu, D. Zheng, Z. Wang, The anodically polarized Mg surface products and accelerated hydrogen evolution, J. Magnesium Alloys 11 (2023) 230–248.
[56] S. Hiromoto, M. Inoue, T. Taguchi, M. Yamane, N. Ohtsu, In vitro and in vivo biocompatibility and corrosion behaviour of a bioabsorbable magnesium alloy coated with octacalcium phosphate and hydroxyapatite, Acta Biomater. 11 (2015) 520–530.
[57] N.T. Kirkland, N. Birbilis, M.P. Staiger, Assessing the corrosion of biodegradable magnesium implants: a critical review of current methodologies and their limitations, Acta Biomater. 8 (2012) 925–936.
[58] A.A. Guangling Song, Matthew Dargusch, Influence of microstructure on the corrosion of diecast AZ91D, Corrosion Sci. 41 (1999) 249–273.
[59] T. Zhang, Y. Li, F. Wang, Roles of β phase in the corrosion process of AZ91D magnesium alloy, Corrosion Sci. 48 (2006) 1249–1264.
[60] H. Feng, S. Liu, Y. Du, T. Lei, R. Zeng, T. Yuan, Effect of the second phases on corrosion behavior of the Mg-Al-Zn alloys, J. Alloys Compd. 695 (2017) 2330–2338.
[61] B. Liu, J. Liu, C. Wang, Z. Wang, S. Min, C. Wang, Y. Zheng, P. Wen, Y. Tian, High temperature oxidation treated 3D printed anatomical WE43 alloy scaffolds for repairing periarticular bone defects: in vitro and in vivo studies, Bioact. Mater. 32 (2024) 177–189.
[62] P.-P. Wu, G.-L. Song, Y.-X. Zhu, Z.-L. Feng, D.-J. Zheng, The corrosion of Al-supersaturated Mg matrix and the galvanic effect of secondary phase nanoparticles, Corrosion Sci. 184 (2021) 109410.
[63] J. Sun, Xue Chen, Kupffer cell-mediated hepatic injury induced by silica nanoparticles in vitro and in vivo, Int. J. Nanomed. (2013) 1129.
[64] F. Cao, G.-L. Song, A. Atrens, Corrosion and passivation of magnesium alloys, Corrosion Sci. 111 (2016) 835–845.
[65] E. Bütev Öcal, Z. Esen, K. Aydınol, A.F. Dericioğlu, Comparison of the short and long-term degradation behaviors of as-cast pure Mg, AZ91 and WE43 alloys, Mater. Chem. Phys. 241 (2020) 122350.
[66] P. Zhao, T. Ying, F. Cao, X. Zeng, W. Ding, Designing strategy for corrosion-resistant Mg alloys based on film-free and film-covered models, J. Magnesium Alloys 11 (2021) 3120–3129.
[67] G.-L. Song, Z. Xu, Effect of microstructure evolution on corrosion of different crystal surfaces of AZ31 Mg alloy in a chloride containing solution, Corrosion Sci. 54 (2012) 97–105.
[68] Z. Zeng, M. Zhou, M. Esmaily, Y. Zhu, S. Choudhary, J.C. Griffith, J. Ma, Y. Hora, Y. Chen, A. Gullino, Q. Shi, H. Fujii, N. Birbilis, Corrosion resistant and high-strength dual-phase Mg-Li-Al-Zn alloy by friction stir processing, Commun. Mater. 3 (2022).
[69] J. Kuhlmann, I. Bartsch, E. Willbold, S. Schuchardt, O. Holz, N. Hort, D. Höche, W. R. Heineman, F. Witte, Fast escape of hydrogen from gas cavities around corroding magnesium implants, Acta Biomater. 9 (2013) 8714–8721.
[70] T. Kraus, S.F. Fischerauer, A.C. Hänzi, P.J. Uggowitzer, J.F. Löffler, A.M. Weinberg, Magnesium alloys for temporary implants in osteosynthesis: in vivo studies of their degradation and interaction with bone, Acta Biomater. 8 (2012) 1230–1238.
[71] X. Li, X. Liu, S. Wu, K.W.K. Yeung, Y. Zheng, P.K. Chu, Design of magnesium alloys with controllable degradation for biomedical implants: from bulk to surface, Acta Biomater. 45 (2016) 2–30.